UNIVERSITY OF CALIFORNIA
RIVERSIDE

Windows to the Brain (WttB): Transparent Nanocrystalline Yttria Stabilized Zirconia Cranial Implants for Non-Invasive, Chronic Access to the Brain for Optical Diagnostics and Therapeutics

A Dissertation submitted in partial satisfaction
of the requirements for the degree of

Doctor of Philosophy

in

Bioengineering

by

Yasaman Damestani

August 2015

Dissertation Committee:
Dr. Guillermo Aguilar, Chairperson
Dr. Huinan Liu
Dr. Masaru P. Rao

The Dissertation of Yasaman Damestani is approved:

Committee Chairperson

University of California, Riverside

Acknowledgments

First and foremost, I would like to thank my advisor, Dr. Guillermo Aguilar for helping me grow as a research engineer. I appreciate all of his contributions, time and ideas that helped make my Ph.D. experience productive and exciting.

This dissertation would not have been possible without our excellent collaborators in Materials Science and Engineering, Dr. Javier Garay and Dr. Yasuhiro Kodera providing us with high-quality samples. I would also like to thank my committee members: Dr. Huinan Liu and Dr. Masaru Rao for brilliant comments and suggestions. I would also like to thank the other members of my oral qualification exam committee: Dr. B. Hyle Park, Dr. Javier Garay, and Dr. Jin Nam, for their time and insightful questions.

The members of *Laboratory of Transport Phenomena for Biomedical Applications* have contributed greatly to my professional time at UC Riverside. My time at UC Riverside was made enjoyable in large part due to many friends and the Association for Women in Science-UC Riverside Chapter that became a big part of my life.

Lastly, I would like to thank my family for all their love, encouragement, and patience. I would like to acknowledge my parents, Fariba and Shahram, who raised me to value reading, critical thinking and problem solving, laying the foundation for my path to a PhD. Thank you to my sister, Rose, for unwavering emotional support and intellectual stimulation. Most importantly, I would like to express my appreciation to Sean for loving, supporting, and leaning in unconditionally.

Dedication

This dissertation is lovingly dedicated to two strong and supportive women, my grandmothers, Fatemeh Sahebi Bazaz and the late Ezatolmolouk Moghadasyan (1921-2014). Thank you for believing in diligence and the pursuit of academic excellence. Your contributions to my life will be felt forever.

ABSTRACT OF THE DISSERTATION

Windows to the Brain (WttB): Transparent Nanocrystalline Yttria Stabilized Zirconia Cranial Implants for Non-Invasive, Chronic Access to the Brain for Optical Diagnostics and Therapeutics

by

Yasaman Damestani

Doctor of Philosophy, Graduate Program in Bioengineering
University of California, Riverside, August 2015
Dr. Guillermo Aguilar, Chairperson

Windows to the Brain (WttB) platform can improve patient care by enabling the delivery and/or collection of light into/from the brain, on demand, over large areas, and on a chronically-recurring basis without the need for repeated craniotomies. WttB holds the transformative potential for facilitating diagnosis and treatment of a wide variety of brain pathologies and neurological disorders including cerebral edema, traumatic brain injury, stroke, glioma, and neurodegenerative diseases.

We have developed a novel transparent nanocrystalline yttria-stabilized-zirconia (nc-YSZ) cranial implant (“window”) that can be used for laser and optogenetic therapy. Since light can be easily transmitted through it without undergoing excessive attenuation—the main obstacle for optical therapy and

diagnostics of deep targets—this material was selected as an excellent candidate. To evaluate the potential of nc-YSZ cranial implants for optical therapy and imaging of the brain, we (1) demonstrated increased photon density in the brain of mice qualitatively and quantitatively with WttB in comparison to native skull using optical coherence tomography; (2) developed drug delivery techniques including micro-needling and application of pneumatic pressure to improve the drug perfusion of optical clearing agents to ex-vivo porcine skin; (3) confirmed the in vivo biocompatibility of nc-YSZ using a dorsal window chamber model; (4) evaluated the bactericidal effect of lasers by imaging of bioluminescent E. coli under WttB.

Table of Contents

List of Figures

Chapter 1. Introduction

Windows to the Brain (WttB) platform can improve patients care by enabling the delivery and/or collection of light into/from the brain, on demand, over large areas, and on a chronically-recurring basis without the need for repeated craniotomies (Figure 1.1). WttB holds the transformative potential for facilitating diagnosis and treatment of a wide variety of brain pathologies and neurological disorders including cerebral edema, traumatic brain injury, stroke, glioma, and neurodegenerative diseases.

According to the Central Brain Tumor Registry of the United States (CBTRUS) report published in 2014, nearly 70,000 new cases of primary brain and central nervous system (CNS) tumors will be diagnosed in the United states this year (2015) [1]. Brain tumors are the second leading cause of cancer death in

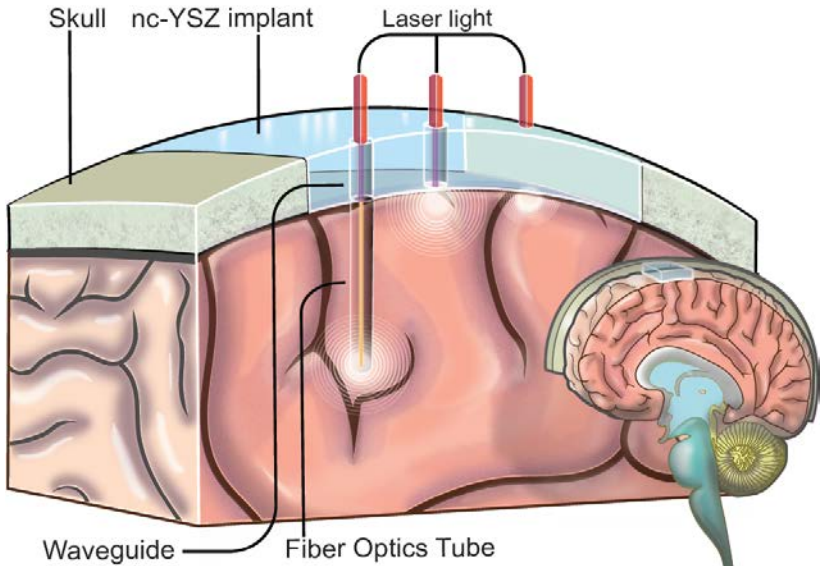

Figure 1.1. Schematic of Windows to the Brain (WttB) Platform

children under 15 years old, and second fastest growing cause of cancer death among people over 65 years old [1]. Currently, the five-year relative survival rate in the U.S. following diagnosis of a primary malignant brain and CNS tumor is 34% [1]. The increase in diagnoses of brain tumors is indicative of improved diagnostic modalities and better access to neurosurgical services [2-5], but it also highlights the necessity of developing effective therapeutic procedures. A silver lining to this gloomy picture is that 95% of recurrences of brain tumors happen within 2 cm of the initial site [6]. Thus, if one could exploit the certainty of the location of remnant and recurring cells to better observe and selectively destroy them during post-operatory therapy, one could positively impact the prognosis and increase the life expectancy of the vast majority of brain tumor patients. Many problems must be overcome in surgical technology before brain tumors can be considered a less threatening form of cancer. One of them, which precludes improvement of post-operatory laser diagnostics and therapy, is the inherent poor transparency of cranial bone and scalp, which limits the spatial resolution and interaction depth that can be achieved with current optical technology.

Craniotomy, removal of part of the skull to access the brain, is performed to remove as much of a tumor as is safe. After the surgery, additional treatment can be used to treat metastatic brain tumors that cannot be surgically removed, and may also be used to prevent metastatic brain tumors from developing. WttB could potentially enable chronic optical monitoring and/or more precisely targeted photodynamic therapy (PDT) of residual tumors [7], which may well prolong

survival and improve quality of life for brain cancer patients. In addition, it could enable non-invasive laser ablation therapies [8] and photothermal therapy with nanoparticles [9], subsequently eliminating the need for recurring craniotomies.

Moreover, based on World Health Organization (WHO) projections, road traffic accidents, the predominant cause of traumatic brain injuries (TBI) will be the third most common creator of global burden of disease (GBD) and disablement by 2020, behind only ischemic heart disease and unipolar major depression [10]. Severe and moderate TBI is a leading cause of mortality and morbidity in industrial countries among children and young adults [11]. 2.5 million cases of TBI occur every year only in the United States, leading to 56,000 deaths while many of its survivors suffer from long-term neurological impairment, costing approximately $56 billion of direct and indirect costs [10, 12, 13]. Replacing the defected skull with WttB during cranioplasty could allow for optical therapy techniques such as low-level laser therapy [14, 15].

Concurrently, optogenetics (chosen as "method of the year" in 2010 by Nature Methods and "breakthrough of the decade" by Science [8]) continues to emerge as a field that combines optics and genetics, opening a new paradigm in neuroengineering. The emergence of optogenetics began in 2005 by demonstration of microbial opsin genes that could safely control neuron activity using different colors of light [16]. Now, optogenetics controls can be delivered—at the speed and with the precision required for biological processing—to specific

brain cells in freely moving mice with substantial adaptability [17], and is studied in over 800 laboratories using animal models and aimed at finding cures for Parkinson's, blindness, depression, narcolepsy, addiction, schizophrenia, and memory [18-26]. In optogenetics, light is transported through optical fibers to achieve gain- or loss- of function of neurons expressing specific photosensitive proteins [26]. TBI could become one of the brain pathologies that could benefit from optogenetic therapy. To aid in this breakthrough, utilizing WttB can help overcome two inherent TBI obstacles: (1) the highly scattering nature of the scalp which attaches to and grows on cranial implants and; (2) the likely existence of multiple affected areas within the brain which must be detected and treated over a prolonged time period, thus limiting the use of optical fibers targeting a single location.

For brain tumor, TBI, and many other brain disorders, optical visualization offers inexpensive, fast, and sensitive guidance on structure, structural abnormalities and therapeutic improvements [27]. These techniques include optical coherence tomography (OCT), laser speckle imaging (LSI), near-infrared (NIR) diffuse optical tomography, and NIR optical imaging with nanoparticle-NIR dye imaging probes [27]. Optical imaging techniques of the brain continue to be hindered by the inability to deliver the necessary light in situ, on demand, over large areas, and on a chronically-recurring basis.

The WttB concept seeks to provide non-invasive chronic optical access to the brain through: 1) replacement of the native skull in regions of interest with an optically-transparent cranial implant; and 2) use of optical clearing agents (OCAs) to temporarily render the overlying scalp transparent on demand. I envision this concept having the potential to enable delivery to and/or acquisition of light from the brain, in real-time, without the need for repeated highly-invasive craniotomies. Such access may also create a new platform for understanding the brain. Furthermore, I envision eventual integration of waveguides within the cranial implants to provide access to deep brain tissues.

Although a number of materials (e.g., titanium, alumina, acrylic, PEEK, etc. [28-32]) have been evaluated for use in cranial reconstruction, none provides the requisite combination of properties required for clinically-viable transparent implants. Yttria-stabilized zirconia (YSZ) represents an attractive alternative in this regard, due to its high strength and toughness [33], well-proven biocompatibility in dental [34] and orthopedic applications [35], and low thermal conductivity [36]. However, YSZ produced using conventional ceramic processing methods is typically opaque, due to scattering induced by micrometer-scale (and larger) internal porosity [37]. This limitation has been circumvented herein through exploitation of the current-activated pressure-assisted densification (CAPAD) process [38]. CAPAD technique enables reduction of internal porosity to nanometric dimensions. At this length scale, porosity is sufficiently small to

minimize scattering in the spectral range of interest for laser-based diagnostics and therapeutics [37].

To evaluate potential for imaging through YSZ-based implants, OCT was used as a representative diagnostic modality, since it provides a unique opportunity for rapid, label-free, and non-invasive “optical biopsy”, i.e. imaging similar in scale and geometry to conventional histology, without the need for physical incision [39, 40]. Using low coherence interferometry to enable detailed 2D and 3D cross-sectional imaging, OCT provides greater spatiotemporal resolution (2-20 μm) than MRI and PET, and greater penetration depth into biological tissue (1-2 mm) than other optical techniques. Recently, the feasibility of using OCT for acute imaging of cortex in thinned skull animal preparations has been demonstrated [41-43]. However, such preparations are not suitable for chronic imaging applications, further motivating the development of the WttB concept.

My preliminary studies, reported in detail in chapter 2, have established the essential feasibility of the WttB concept by demonstrating the possibility for optically interrogating shallow brain tissues through our transparent cranial implants in an acute murine model [44, 45]. They have also garnered significant media attention, including recent coverage by prominent news organizations such as *BBC News, Google News, MSN,* and many others [46].

For cranial implants to be successful as optical “windows” for post-operatory and prolonged diagnostics and/or therapy, skin (scalp) scattering must be overcome. It is in this context that optical cleating agents (OCAs) can play an important role, as they may be applied topically to the skin to reduce scattering locally, temporarily and reversibly, prior to laser irradiation. While OCAs have been readily used to enhance a number of optical diagnostic techniques [47-52], including OCT [53, 54], need still exists for development of a means for delivering OCA in a clinically-relevant and efficacious manner. In most early studies, *ex vivo* skin samples were simply immersed in OCA, which is not possible *in vivo*. Moreover, the highly viscous and water soluble nature of OCAs precludes appreciable penetration through the stratum corneum during topical application. Finally, subdermal injection has shown to be limited by non-uniform distribution and inflammation [53, 55, 56].

Therefore, in parallel, I studied optical clearing of the scalp by performing combinations of various techniques to enhance optical clearing agent (OCA) perfusion; including heating of OCA, microneedling and/or application of pneumatic pressure over the skin surface being treated (vacuum and/or positive pressure). Briefly, I demonstrated that the combination of heated OCA, microneedling and vacuum pre-treatment with positive pressure-post treatment combined to significantly enhance the perfusion of topically applied PG. The details of these studies are reported in Chapter 3. Although further studies are required to evaluate the efficacy of combined perfusion enhancement techniques in vivo, the

current results suggest promise for helping facilitate the translation of OCA to the clinic [44].

Although conventionally-processed microcrystalline YSZ (mc-YSZ) has well-proven biocompatibility in dental and orthopedic applications [33], thorough assessment within the context of cranial implants is lacking and is necessitated by the environment's unique demands (e.g. intracranial pulsatility, cerebrospinal fluid exposure, etc.). Biocompatibility assessments for nc-YSZ are also lacking, and must be considered due to the unique properties associated with nanocrystallinity (e.g. increased surface energy). The prolonged inflammatory response to an implant is one of the primary causes of failure to integrate into tissue. In Chapter 4, I investigated the inflammatory and angiogenic host tissue response to nc-YSZ for two weeks using a hamster dorsal skinfold chamber model. Intravital fluorescence microscopy of host tissue revealed no significant change in microhemodynamics, microvascular permeability, and leukocyte-endothelial cell interaction.

Bacterial adhesion to the cranial implant must also be considered, as it is the leading factor for biofilm formation (fouling), infection, and treatment failure. Also, bacterial adhesion to the implant and biofilm formation could limit transmittance through WttB implants and consequently decrease its usefulness for optical imaging and therapy. E. coli, in particular, is the most common isolate in gram-negative bacillary meningitis after cranial surgery or trauma. In Chapter 5, I

demonstrated the potential of using nc-YSZ as a cranial implant to allow locally selective, non-invasive, chronic treatment of bacterial layers (fouling) that might form under cranial implants without causing adverse thermal damage to the underlying host tissue when appropriate laser parameters are used.

My dissertation research will pave the way for the development of a new area of laser therapy and imaging of the brain using this unique biomechanically stable transparent cranial implant. Replacing portions of the skull to allow non-invasive optical interrogation of the brain in an ongoing recurring basis, i.e. the WttB platform, is the primary integrative technology goal of the project. The outcomes will also advance the fundamental knowledge and capabilities of diagnostic and therapeutic modalities in neurosurgical and orthopedic fields. My dissertation research may serve as a critical enabler for the recently announced BRAIN Initiative, by providing means for extending optical neurotechnologies, such as optogenetics, to chronic studies in human subjects.

Chapter 2. Transparent Nanocrystalline Yttria-Stabilized-Zirconia Calvarium Prosthesis

Background

Laser-based techniques have shown promise for enhancing the diagnosis and treatment of many neurological disorders, including cerebral edema, stroke, and cancer, among others [57-59]. However, the poor transparency of cranial bone to clinically-relevant laser wavelengths (i.e. λ = 550 - 1300 nm) typically necessitates use of invasive craniectomies to provide optical access to the brain. This constrains the ultimate utility of such techniques, particularly for applications where chronically-recurring access over large areas is required.

Recent studies have demonstrated potential for increasing cranial transparency through thinning [60, 61]. However, since this diminishes protection for the brain, associated safety concerns may preclude opportunity for translation of such techniques to the clinic. Other studies have reported use of transparent glass-based implants, either in place of cranium [62], or as an overlay to increase the rigidity of thinned-skull preparations [63]. However, the extremely low fracture toughness of typical glasses (K_{IC} = 0.7 – 0.9 MPa·$m^{1/2}$) increases potential for catastrophic failure by fracture, which will limit opportunity for use of such implants beyond the laboratory. This, therefore, motivates the search for alternate materials that will provide better potential for eventual clinical use.

While a number of synthetic materials have been evaluated for use in calvarial reconstruction, including titanium, alumina, and acrylic [28], none provide the requisite combination of transparency and toughness required for clinically-viable transparent cranial implants. Yttria-stabilized zirconia (YSZ) represents an attractive alternative, due to its relatively high toughness (K_{IC} ~ 8 MPa·$m^{1/2}$), as well as its proven biocompatibility in dental and orthopedic applications. However, YSZ is typically opaque, thus precluding its consideration thus far.

Herein, we report the preliminary evaluation of novel transparent nanocrystalline YSZ (nc-YSZ) cranial implants that seek to provide new opportunity in this regard. Using optical coherence tomography (OCT), we demonstrate the initial feasibility of nc-YSZ cranial implants within the context of cortical imaging in an acute murine model. We then discuss the implications of these implants with regard to a broader concept we are developing, which may eventually serve as a critical enabler for the wider use of lasers in the diagnosis and treatment of neurological disorders.

Methods

The transparent nc-YSZ cranial implants were made possible through use of the CAPAD process [38], an emerging technique that enables reduction of internal porosity to nanometric dimensions, and thus, reduction of the optical scattering that renders typical YSZ opaque [37].

Transparent nc-YSZ Cranial Implant Fabrication

The current-activated pressure-assisted densification (CAPAD) process relies upon simultaneous application of high mechanical pressure and electric current, the latter of which being the uniquely distinguishing feature. The current serves as the sole source of heating, which allows high heating and cooling rates, as well as good temperature uniformity. When coupled with the increased surface energy driving force produced by pressure [64], this allows rapid densification of nanocrystalline materials at temperatures far below conventional methods, as well as reduction of internal porosity to nanometric dimensions. Details of the manufacturing process have been reported earlier [65].

The transparent nc-YSZ cranial implants used in this study were fabricated using the CAPAD process to densify commercially-available nanocrystalline YSZ powders with a reported crystallite size of 50 nm (ZrO_2-8 mol% Y_2O_3, Tosoh Corporation, Tokyo, Japan). The YSZ powders were loaded into a graphite die with a 19 mm inner diameter and densified to form transparent nc-YSZ blanks with thicknesses ranging from 0.2 – 1.0 mm, average grain size of 55 nm, and relative density > 99% (Process conditions: Maximum temperature = 1200 °C, maximum pressure = 141 MPa, and total processing time = 17 min). The blanks were then polished using silicon carbide and diamond abrasives. The blanks were subsequently annealed at 750 °C in air to reduce oxygen vacancy concentration, thus reducing absorption and improving transparency [37]. For the *in vivo* imaging

studies, 2.1 x 4.2 x 0.2 mm^3 rectangular implants were machined from the annealed blanks using diamond abrasive cutting.

Figure 2.1 shows the absorption spectra of the transparent nc-YSZ over the wavelength range of interest for most clinical applications (i.e. λ = 400- 1500 nm). This measurement was performed with a spectrophotometer (Cary 500, Varian, Inc., Palo Alto, CA) which generates single wavelengths with accuracy of ±0.02 nm. This plot clearly shows minimal absorption within the wavelength range of interest for the OCT imaging used in this effort (~1300 nm), as would be expected based on the imaging performance demonstrated in the original manuscript.

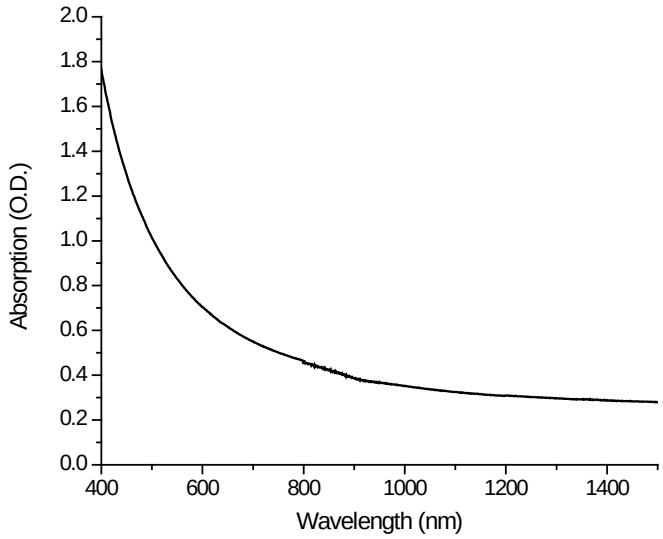

Figure 2.1. Nc-YSZ absorption spectra

Densified nc-YSZ blanks were polished, annealed, and machined into rectangular implants with dimensions of 2.1 x 4.2 x 0.2 mm^3. Figure 2.2A demonstrates the transparency of the finished implants.

In preparation for surgery, female CD1 mice between the ages of 6-8 weeks were anesthetized intraperitoneally with a combination of ketamine and xylazine (80 mg/kg ketamine/10 mg/kg xylazine). The animals were then placed on a homeothermic pad to ensure optimal body temperature of ~37 °C and additional anesthetic was administered as necessary. Ophthalmic ointment was applied over the eyes, and hair was removed using clippers and depilatory cream. Finally, the nc-YSZ implants were cleaned with acetone and 70% ethanol, followed by autoclaving at 121 ^oC for 30 min for sterilization.

Once prepared, the mice were immobilized in a stereotactic frame. A midline incision was then made and the scalp retracted to expose the skull. Right-side craniectomies equivalent to the dimensions of the nc-YSZ implants were then performed with the *dura mater* left intact. Finally, the nc-YSZ implants were placed over the exposed brain and affixed to the surrounding skull with dental cement. In all studies, imaging was performed immediately after surgery, and all animals were sacrificed immediately after imaging by anesthesia overdose.

As shown in Figures 2.2B – 3D, right-sided craniectomies were performed on anesthetized mice, followed by fixation of nc-YSZ implants to the surrounding skull with dental cement. The left-side of the cranium was left unmodified to serve as a control. All animal experiments were conducted under a protocol approved by the University of California, Riverside Institutional Animal Care and Use Committee (#2010-0018), and in conformance with the *Guide for the Care and Use of*

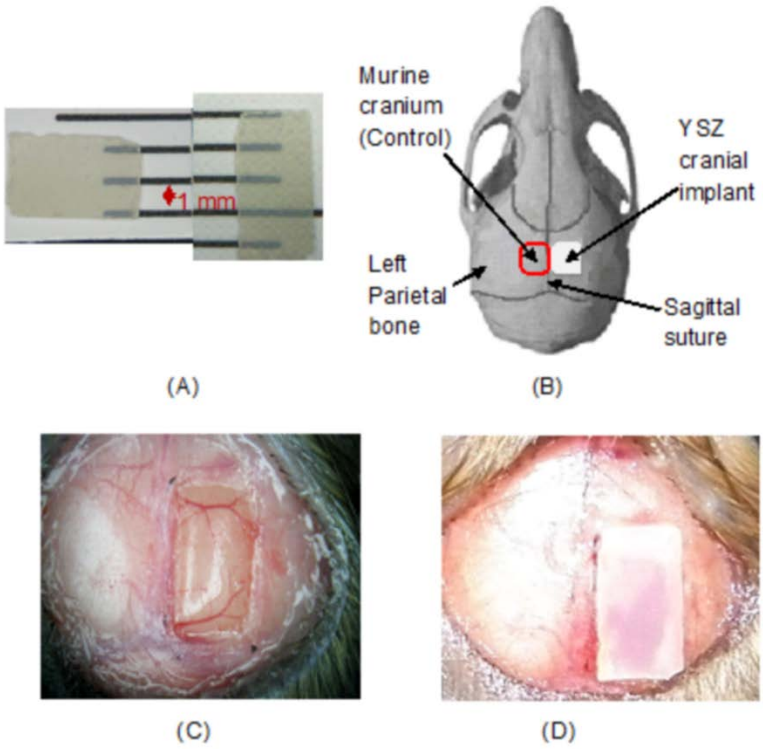

Figure 2.2. Transparent nc-YSZ cranial implants: A) Photograph of implant placed on printed scale to demonstrate transparency; B) Schematic of craniectomy location on murine cranium; C) Photograph of craniectomy with dura mater left intact; and D) Photograph after implant placement. Note: Implant opacity in (D) is flash-induced image artifact.

Laboratory Animals published by the National Institutes of Health (NIH Publication No. 85-23, revised 1996).

In vivo OCT Imaging

OCT was used as a representative optical imaging modality in the present study to evaluate the initial feasibility of nc-YSZ cranial implants for optical diagnostic applications. OCT's use was motivated, in part, by the opportunity it provides for rapid, label-free, and non-invasive "optical biopsy" [40], as well its greater penetration depth (1-2 mm) relative to other optical techniques, such as two-photon or confocal microscopy [66, 67]. However, while such depths may be sufficient for some applications, others will require deeper access, particularly since many pathologies can present well beneath the cortical surface. To this end, it is conceivable that nc-YSZ implants could also be compatible with deeper penetrating optical techniques, such as photoacoustic tomography; however, confirmation of this is beyond the scope of this preliminary effort.

Using low coherence interferometry, OCT forms depth-resolved images of biological tissue by measuring the magnitude and delay of backscattered light from varying depths within the sample, thus enabling detailed 2D and 3D cross-sectional imaging. Details of the spectral domain OCT system used in this work have been reported previously by Wang et. al. [42]. Briefly, a broadband light source composed of two super-luminescent diodes (SLDs) was used. The SLDs have a combined center wavelength of 1298 nm and 120 nm full-width at half

maximum (FWHM) bandwidth, which is split between the sample arm and reference arm. The backscattered light in each arm recombines at the splitter and passes through a diffraction grating. The resulting spectrum is collected by two line scan cameras with an acquisition rate of 15 kHz, and a Fourier transform of the spectrum produces a single A-line. Lateral scanning of the focused optical beam (10 μm spot size, 6 mW incident power) across the sample produces two-dimensional images. In the present study, the axial resolution was approximately 8 μm, and the transverse resolution was 20 μm. Each image was composed of 2048 A-lines. The data acquisition software was written in C++, and post-processing was performed using MATLAB.

OCT Image Interpretation

In the OCT intensity image presented in Figure 2.3, the black and white regions represent those with high and low backscattered light intensity, respectively, whereas discrete dark lines represent focal scattering at sharp interfaces between regions of significantly different refractive index. Cranial thickness is evidenced by the dark mottled band at the top of the image (left of midline), which arises due to scattering induced by heterogeneous bone microstructure. Conversely, nc-YSZ implant thickness is evidenced by the lighter region bounded by parallel dark lines at the top of the image (right of midline).

This demonstrates that there is minimal scattering within the bulk of the nc-YSZ implant and only focal scattering at the upper and lower tissue-implant

interfaces. Moreover, increased signal strength when imaging through the nc-YSZ implant is clearly evidenced by the presence of the diffuse darker band near the bottom of the image. This band represents sub-cortical white matter, which appears darker due to increased backscattering arising from its greater myelination [68, 69]. The absence of such structures when imaging through native cranium further confirms the enhanced optical imaging capability afforded by the nc-YSZ implants.

The OCT signal strength data presented in Figure 2.3 represents the integrated backscattered signal intensity (log scale) as a function of depth from the cortical surface for the intensity image shown in Fig. 2.2. At every depth, there is significantly greater signal strength when imaging through the nc-YSZ implants relative to native cranium. This, therefore, further demonstrates the enhanced

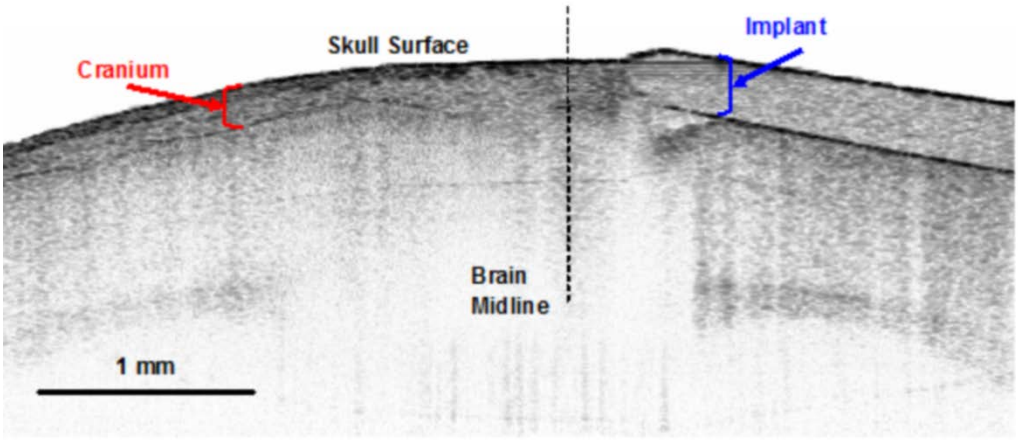

Figure 2.3. OCT cross-sectional image of murine brain (coronal view through: (Left) Native cranium; and (Right) nc-YSZ implant.

transparency, and thus, the improved imaging performance afforded by the nc-YSZ implants.

Results

Figure 2.3 shows cross-sectional OCT images of murine brain through native cranium (left of midline) and nc-YSZ implant (right of midline) in the same animal. Detailed description of the image interpretation is presented in the *Supplemental Materials.* The enhanced transparency of the nc-YSZ implant is evidenced by the opportunity it provides for imaging of sub-cortical white matter (darker band at bottom of image, right of midline), which is nearly imperceptible when imaging through native cranium (left of midline).

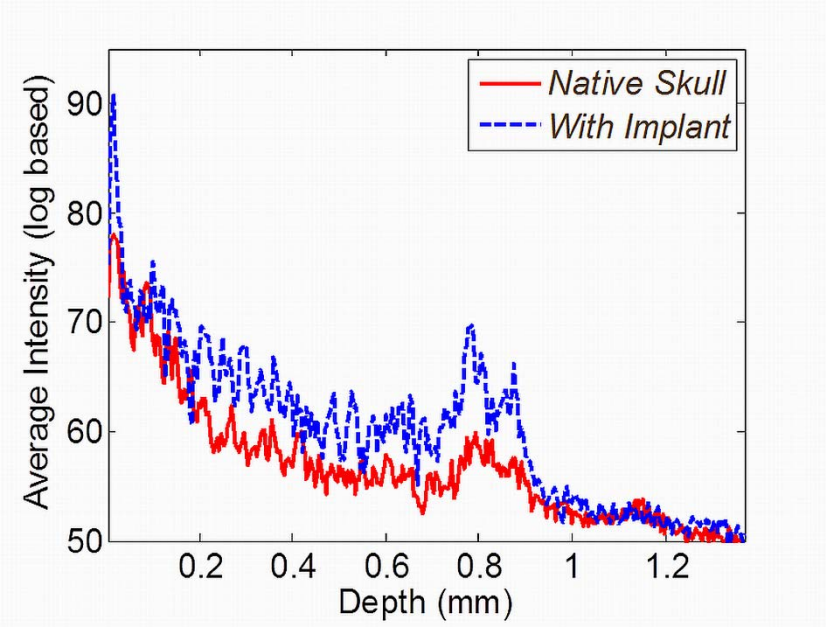

Figure 2.4. OCT signal strength depth profile for imaging through native cranium vs. nc-YSZ implant.

Figure 2.4 shows OCT signal strengths as a function of depth from the cortical surface when imaging through native cranium and nc-YSZ, respectively. As would be expected, intensity decays with depth for both, aside from the increase associated with sub-cortical white matter. However, signal strength at nearly every depth is significantly higher when imaging through the nc-YSZ implant, further demonstrating the enhanced imaging performance.

Discussion

Figures 2.3 and 2.4 demonstrate that OCT imaging through nc-YSZ implants is indeed possible and provides greater signal strength than imaging through native cranium. This, therefore, establishes the initial feasibility of nc-YSZ as a transparent cranial implant material for optical diagnostic and therapeutic applications. Moreover, when coupled with the high toughness of nc-YSZ, this suggests unique potential for eventual clinical application.

However, before such potential can be realized, further studies are required to evaluate the long-term biological response to nc-YSZ implants, since: a) the demands imposed upon cranial implants differ from those in dental and orthopedic applications; and b) the need for transparency will require minimization of fibrosis and/or bone regrowth over the implant. Regarding the latter, it may ultimately be more beneficial to thin the cranium significantly and then cover with a nc-YSZ implant, as Shih et al. recently demonstrated for glass-based implants [66].

Although beyond the scope of the current study, it is important to also briefly consider the effect of the scalp on imaging performance, since: a) coverage of the nc-YSZ implant with native scalp will be preferred for applications requiring long-term implantation; and b) repeated scalp removal is unlikely to be desirable when chronically-recurring access over large areas is required. Optical clearing agents (OCAs) represent a compelling possibility in this regard, since they have been shown to provide capability for temporarily rendering skin transparent on demand [54, 70-72]. When used in conjunction with nc-YSZ implants, we envision potential for realization of an innovative new concept we have named Windows to the Brain (WttB), which seeks to eventually provide opportunity for optical accessing the brain, on-demand, over large areas, and on a chronically-recurring basis, without need for repeated craniectomies or scalp removal.

While the current study represents only the first step towards realization of the WttB concept, it is instructive to consider the opportunities this may eventually afford. For example, opportunity may arise for chronic monitoring of cerebral edema, which is largely precluded by the invasiveness of current techniques [73]. Similarly, it may enable chronic monitoring and more precise targeting of photodynamic therapies for residual gliomas [74], which could prolong survival and improve quality of life for many suffering from brain cancer. Finally, it could provide a platform for development of new optical neuromodulation modalities, with potential applications ranging from fundamental neurophysiology studies to clinical psychiatry [75].

Acknowledgments:

I would like to acknowledge the contribution of my co-authors to this study: Dr. Carissa Rodriguez, Jenny Szu, Mike Hsu, Dr. Yasuhiro Kodera, Dr. Devin Binder, Dr. Hyle B. Park, Dr. Javier E. Garay, Dr. Masaru P. Rao, and Dr. Guillermo Aguilar. I thank Dr. Melissa Eberle for her contribution to OCT data collection, and Dr. Elaine D. Haberer and Dr. Mohammad Shahriar Zaman for their contribution to the absorption measurement.

Chapter 3. Optical Clearing Agent Perfusion Enhancement via Combination of Heating, Microneedling, and Pneumatic Pressure

Introduction

Optical Clearing Agents (OCAs) are nonreactive hyperosmotic agents that are used to increase tissue transparency in a transient and reversible manner. Although the exact mechanisms are still not well understood, prevailing opinion suggests that clearing is achieved through reduced optical scattering arising from matching of OCA and tissue refractive indices (due to OCA ingress and water egress under osmotic pressure), and/or dehydration and ordering of tissue fibrils in the dermis [48, 54, 71, 76]. By providing means for transiently clearing skin, OCAs have shown promise for enhancing the performance of a variety of diagnostic techniques, such as optical coherence tomography [53, 54], second harmonic generation microscopy [47, 48], confocal microscopy [47, 48] and two-photon excited fluorescence microscopy [49-52], as well as many other medical applications [53, 71, 72, 77-83]. Optical clearing also represents a critical element of a new concept we have recently introduced, Windows to the Brain. In this concept, OCAs would allow transient clearing of the scalp overlying a transparent cranial implant, thus providing a minimally-invasive means for optically accessing the brain, on-demand, over large areas, and on a chronically-recurring basis, without need for repeated craniectomies [45].

However, despite this promise, the continuing lack of sufficiently effective and/or practical OCA perfusion techniques *in vivo* represents a limitation with regard to clinical translation. The high viscosity of OCAs results in poor penetration through the stratum corneum when applied topically, as well as slow perfusion within the epidermis. In *ex vivo* studies, rapid and effective clearing has only been achieved through complete immersion of excised tissue samples in OCA, which is not feasible for use *in vivo* [49-52]. Single dose subdermal injection has been shown to produce fast clearing *in vivo*; however, this has been accompanied by necrosis and scarring, thus limiting the utility of this technique [84]. Sonophoresis and application of 1500 μm microneedles have shown potential for increasing clearing relative to topical application of OCA alone; however, visible damage to the stratum corneum was observed [85]. Finally, removal of the stratum corneum via sandpaper abrasion has been shown to enhance the transdermal delivery of OCA [86]; however, inflammation was also observed.

Herein, we report the first systematic and quantitative study of OCA perfusion enhancement using various combinations of OCA heating, microneedling pre-treatment (i.e., prior to OCA application), vacuum pre-treatment (i.e., prior to OCA application), and/or positive pressure post-treatment (i.e., after OCA application). The motivation for OCA heating was based on recent studies demonstrating enhanced clearing performance with heating of glycerol up to 40-45^{o}C [87]. Moritz et. al. has previously studied time-surface thresholds for thermal injury of human skin and demonstrated that two hours of exposure to 45 ^{o}C at the

surface of human skin has caused hyperemia without loss of epidermis. For this study, the exposure time of 45 ^{o}C OCA to skin was limited to 30 minutes [88]. As such, epidermal loss is not expected, although hyperemia could still occur in vivo. The rationale for microneedling was based on the presumption that this would produce shallow pores that enable circumvention of the stratum corneum in a minimally-invasive manner. The rationale for vacuum pre-treatment was based on the presumption that the resulting tissue stretching could enlarge pores produced by prior microneedling and therefore increase the OCA perfusion [89, 90]. Finally, the rationale for positive pressure post-treatment was based on the presumption that this could increase OCA flux through pores produced by prior microneedling.

Materials and Methods

Skin Preparation

Ex vivo abdominal porcine skin with intact stratum corneum was used for all studies, due to its anatomical similarity to human skin [91]. Fresh skin was obtained from a local research facility (University of California Irvine, Department of Surgery). Upon receipt, the tissue was sealed to prevent dehydration and stored at 4 ^{o}C. All tissues were used within two weeks of receipt. Prior to each experiment, the skin samples were thawed and the subcutaneous fat layer was removed to yield samples of 1.5 mm ± 0.1 mm thickness, which included stratum corneum (26.4 ± 0.4 μm thickness [92]), epidermis (65.8 ± 1.8 μm thickness [92]), and dermis (balance of sample thickness). The prepared samples were then re-

hydrated by immersion in room temperature (RT) saline for 30 min. For all experiments, RT was maintained at 18 ^{o}C and relative humidity at 30%.

OCA Perfusion

While a number of hyperosmotic agents have shown potential for use as OCAs, Propylene glycol (PG) (Sigma-Aldrich, USA) was selected for the current studies, due its superior permeability [93, 94]. In all experiments, 100 µL of PG was applied topically over an area of approximately 100 mm^2, and total PG exposure time was maintained at 30 min. *30 min was chosen on the basis of decreasing clearing rate as well as maintaining the experiment parameters within the context of eventual clinical practicality.* For studies involving RT OCA, PG was dispensed from a container held under ambient conditions (18 ^{o}C). For studies involving heated OCA, PG was warmed to 45 ^{o}C using a hot plate prior to topical application. This temperature was selected to minimize PG viscosity (16.4 mPa·s at 44 ^{o}C vs. 46.4 mPa·s at 24 ^{o}C [95]) without surpassing the threshold for thermal damage to the skin.

For studies involving microneedling pre-treatment (i.e., prior to OCA application), a commercial microneedle roller was manually applied to the skin samples in 0, 45, and 90 degree rolling directions over the same area, with thirty roller passes were applied in each direction (CR2 MTS roller, Clinical Resolution

Laboratory, Brea, CA; ISO 13485:2003 approved, microneedle length = 0.2 mm, diameter = 0.07 mm, and pitch = 2.5 mm). The pore density produced by

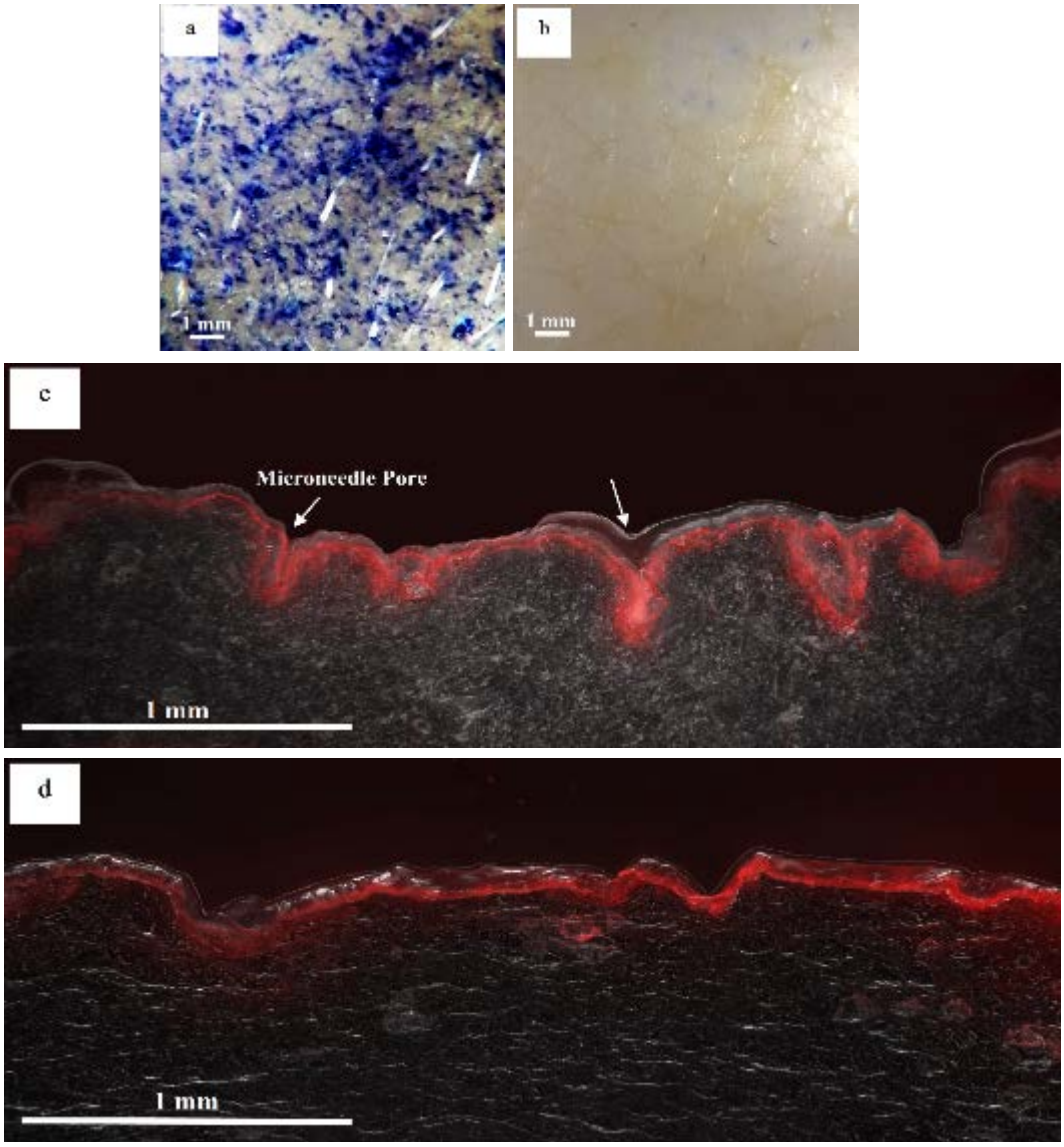

Figure 3.1. Characterization of ex vivo porcine skin treated with 200 µm microneedle roller: a) Digital photograph of microneedled skin demonstrating average pore density of 240 ± 10 pores/cm^2; b) Digital photograph of untreated control skin; c) Histological cross section of microneedled skin demonstrating higher optical intensity due to higher perfusion of Rhodamine R compared to untreated tissue (Figure 1d) and average pore diameters of 0.22 ± 0.08 mm on the surface of skin, and average pore depths of 0.20 ± 0.04 mm; and d) Histological cross section of non-microneedled skin demonstrating native topographical variation.

microneedling (Figure 3.1a) was measured via topical dye application (trypan blue), followed by removal of excess dye, and finally, imaging with a Dermatoscope (3.5V Pro-Physician Dermatolight-LED Dermatoscope) coupled with a digital camera (Kodak MAX Z990). Untreated (i.e., non-microneedled) tissue specimens were processed in a similar manner to serve as control (Figure 3.1b). The depth and diameter of pores produced by microneedling (Figure 3.1c) was measured by topical application of Rhodamine R, followed by histological sectioning and imaging an average of twenty 40 μm thick slices per sample with a fluorescence microscope (Leica MZIII Pursuit). In each tissue section, an average of 6 pores were measured in randomized locations across the section, and measurements were only taken for pores with clearly defined boundaries (i.e. sharp demarcation between Rhodamine R (red) and the adjacent background (black)). Since many pores tapered with depth into the skin, the reported pore diameters are those measured at the skin surface. Collectively, these measurements indicated average pore densities of 240 ± 10 pores/cm^2, average pore diameters of 0.22 ± 0.08 mm on the surface of skin, and average pore depths of 0.20 ± 0.04 mm for microneedled skin. Histological imaging of non-microneedled skin samples was also performed to characterize the native topographical variation of the skin (Figure 3.1d).

For studies involving pneumatic pressure, a custom apparatus (Figure 3.2a) was fabricated from transparent acrylic to allow application of pressure (negative or positive) to the epidermal surface of the skin samples. During these studies,

sample hydration was maintained from the dermal surface via contact with an underlying body-temperature, saline-saturated, rigid foam block (Oasis Wet Floral Foam, Smithers-Oasis North America, Kent, OH).

For studies involving vacuum pre-treatment (i.e., prior to OCA application), vacuum ranging from 17 kPa to 50 kPa was applied for 1 min using a hand pump (9963K21, McMaster-Carr, Los Angeles, CA). For studies involving positive

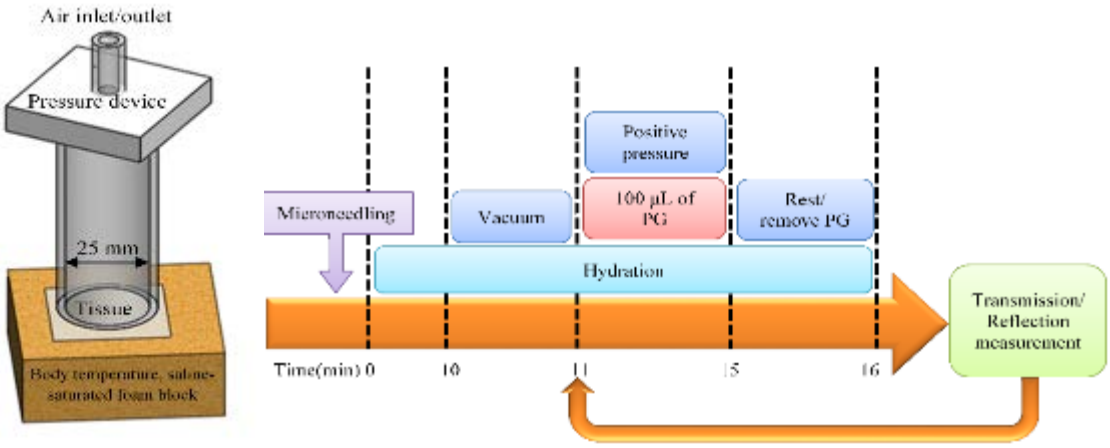

Figure 3.2. a) Schematic of apparatus used for pneumatic pressure OCA perfusion enhancement studies in *ex vivo* porcine skin. Tissue samples were placed within the apparatus such that their dermal surface was in contact with the underlying body-temperature, saline-saturated foam block, while the epidermal surface was exposed to vacuum and/or positive pressure; and b) Block diagram illustrating the sequence of operations for application of the various PG perfusion enhancement techniques. Briefly, the hydrated porcine skin was treated with microneedles and was kept hydrated from the dermis side using a body temperature, saline-saturated foam block for 10 min before the start of each experiment. For studies involving vacuum pre-treatment, vacuum was applied for 1 min. For studies involving positive pressure post-treatment, pressure was applied for 4 min after the PG application. The tissue was rested for 1 min, and PG was removed before the measurement of optical properties (Transmission/Reflection). The steps including the PG and positive pressure post-treatment application, rest and removal of PG, and the measurement of optical properties were repeated for 30 min (6 times).

pressure post-treatment (i.e., after OCA application), pressures ranging from 35 kPa to 172 kPa were applied for 4 min using house compressed air with a regulator to control pressure (Harris Gas Regulator, Harris Products Group, Gainesville, GA)

Optical Clearing Characterization

After application of prescribed perfusion enhancement protocols, residual PG was removed from the skin surface by gentle wiping with an absorbent cloth, and the samples were immediately transferred to an optical measurement system. Transmittance and reflectance spectra across wavelengths ranging from 450 – 850 nm were measured using a fiber optic spectrometer (SD2000, Ocean Optics, Dunedin, FL). A fiber optic bundle with a 150 Watt quartz halogen illuminator was used as the light source for transmission measurements (Model 180, Fiber-Lite, Dolan Jenner, Boxborough, MA). Reflection was measured with a Spectralon coated integrating sphere with a built-in tungsten-halogen light source for 400 - 800 nm wavelengths (ISP-REF Integrating Sphere, Ocean Optics). The system was calibrated using a diffuse reflectance standard (WS-1, Ocean Optics). Measurements were made every five minutes for 30 min total, and all experiments were repeated in triplicate (Figure 3.2b).

Wavelength Selection

Specific attention was focused on optical response at the following wavelengths due to their relevance for various laser-based medical imaging and

therapeutic modalities: 1) 532 nm for laser-induced photoacoustic brain imaging [96]; 2) 630 nm for photosensitizer activation in photodynamic therapy of brain tumors [97]; 3) 650 nm for near-infrared spectroscopy and topographical imaging of brain [98]; 4) 670 nm for emerging photochemical internalization (PCI)-enhanced nonviral gene-directed enzyme prodrug cancer therapy[99]; and 5) 810 nm for brain interstitial laser photocoagulation therapies [100].

Data Analysis

Normalized transmittance, *NT*, was calculated using,

$$NT = \frac{T_t}{T_o} \quad (1)$$

where T_t was the transmittance of the skin sample measured at time *t* after completion of a prescribed OCA treatment protocol, and T_o was the transmittance measured before application of the prescribed OCA treatment protocol (i.e., untreated skin baseline transmittance). The reduced scattering coefficient, μ_s', which combines the transmittance, reflectance, and thickness of the sample, was calculated using Prahl's inverse adding-doubling algorithm.

$$\mu_s' = \mu_s (1-g) \ [cm^{-1}] \quad (2)$$

In these calculations, the anisotropy factor was assumed to be 0.9 for skin in the visible and NIR spectral range, and μ_s represented the scattering coefficient [101].

Finally, the photon penetration depth, δ, was estimated using the following expression [102]:

$$\delta = \frac{1}{\sqrt{3\,\mu_a\,(\mu_a + \mu_s')}} \quad (3)$$

where μ_a represented the absorption coefficient at the measured wavelength, which was also calculated using the Prahl's inverse adding-doubling algorithm.

Statistical Analysis

All data was statistically analyzed using two-way repeated-measures ANOVA and Bonferroni post-tests. Statistics were calculated using a commercially-available software package (Prism 5.0, GraphPad, San Diego, CA). Changes were considered statistically significant when the *P* value was less than 0.05.

Qualitative Demonstration of Optical Clearing Efficacy

To provide a qualitative demonstration of the efficacy of optical clearing in skin treated with the optimal PG perfusion enhancement protocol, we utilized a thermocavitation technique we reported previously [103, 104]. Briefly, treated *ex vivo* porcine skin was placed on the outer face of a quartz cuvette containing saturated aqueous copper nitrate solution ($CuNO_4$). The skin was then irradiated with an 810 nm CW laser operating at 12W. Laser transmission through the cleared skin caused thermocavitation-induced bubble formation in the $CuNO_4$

solution, which was captured using a high speed video camera recording at 10^5 frames per second (Phantom V7, Version9.1). Control experiments consisting of untreated skin subjected to identical conditions were also performed.

Results and Discussion

Variation of Transmittance with Time

Figure 3.3 shows the variation of *NT* with time after topical application on *ex vivo* skin samples with RT PG. The change in *NT* is significantly different after 20 min for some wavelengths and after 30 min for all wavelengths ($P < 0.05$). The statistical analysis indicates the effect of time was extremely significant ($P < 0.001$) and the effect of wavelength was very significant ($P < 0.01$), with more pronounced improvement at shorter wavelengths. Maximum *NT* was observed at 30 min for

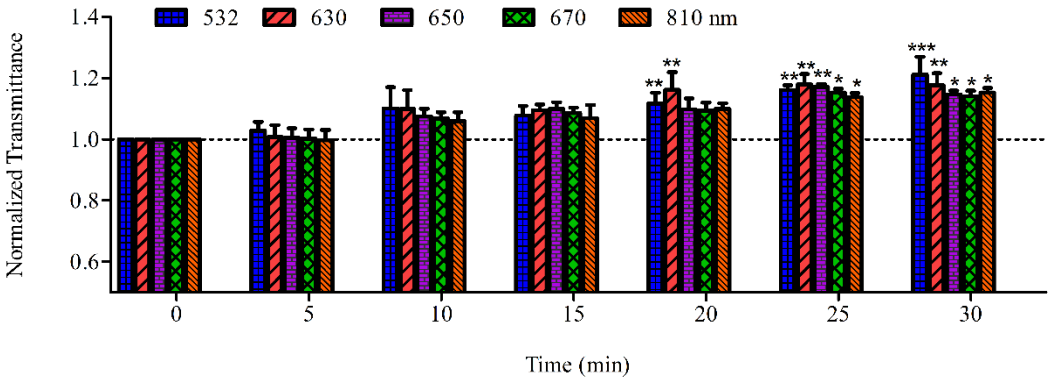

Figure 3.3. Variation of NT at various medically-relevant laser wavelengths with time after treatment of hydrated, ex vivo porcine skin with room temperature propylene glycol (PG). All data are normalized by transmittance for each skin sample before PG application (i.e. untreated skin). N = 3 for each condition and error bars represent 1 standard deviation, 2-way ANOVA repeated measures, Bonferroni post-test *$P < 0.05$, **$P < 0.01$, ***$P < 0.001$ relative to 0 min.

most wavelengths, with up to 21% improvement relative to untreated skin ($P < 0.05$). Based on this preliminary study, measurement time of 30 min after treatment was selected for subsequent perfusion enhancement studies. The relatively modest increase in *NT* confirms the strong barrier function of the stratum corneum, which precludes significant clearing with topical RT PG alone.

Figure 3.4 shows the variation of *NT* with time after treatment of microneedled skin with RT PG. The change in *NT* is significantly different after 30 min for all wavelengths ($P < 0.05$), thus supporting the appropriateness of this measurement time point for subsequent microneedling-based perfusion enhancement studies. Interestingly, only minimal enhancement of transmittance was observed relative to RT PG alone (i.e., Figure 3.3). Moreover, the effect of microneedling seemed to be more pronounced for longer wavelengths, although

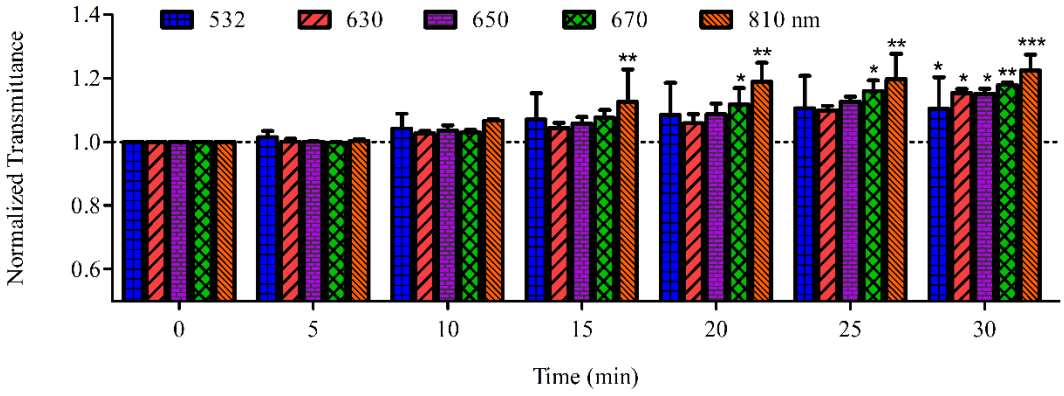

Figure 3.4. Variation of NT with time after treatment of microneedled skin with room temperature PG. All data are normalized by transmittance for each skin sample before pre-treatment with microneedles (i.e. untreated skin). N = 3 for each condition and error bars represent 1 standard deviation. 2-way ANOVA repeated measures, Bonferroni post-test *$P < 0.05$, **$P < 0.01$, ***$P < 0.001$ relative to 0 min.

the underlying cause is unclear. While other studies using the same region of skin (abdominal) as in this study have shown up to two-fold increase in NT with microneedling [105], this may due to the longer needle length used in those studies (i.e. 500 μm microneedle roller vs. 200 μm for the current study). While both needle lengths are sufficient to circumvent the stratum corneum and access the epidermis, longer needles may produce deeper pores, which could facilitate OCA perfusion. However, longer needles may also increase pain sensation, thus producing a potential tradeoff between clearing efficacy and invasiveness when used in vivo.

Variation of Transmittance with Vacuum Pre-treatment Pressure

Figure 3.5 shows the variation of *NT* with vacuum pre-treatment pressures for microneedled skin treated with RT PG, all 30 min after treatment. The data

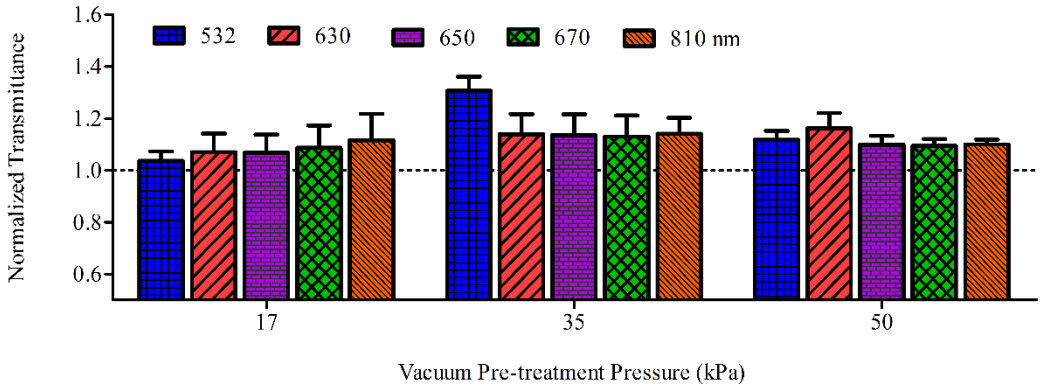

Figure 3.5. Variation of transmittance with vacuum pre-treatment pressures for microneedled skin treated with room temperature PG. Measurements were made 30 min after treatment, and all data are normalized by transmittance for each skin sample before pre-treatment with vacuum and microneedles (i.e. untreated skin). N = 3 for each condition and error bars represent 1 standard deviation. 2-way ANOVA repeated measures, Bonferroni post-test **P* < 0.05, ***P* < 0.01, ****P* < 0.001 relative to 17 kPa. The *NT* results with different vacuum pre-treatment pressures for RT PG are not significantly different (*P* > 0.05).

showed no statistically significant variation in *NT* with vacuum pre-treatment pressure ($P > 0.05$). This suggests that minimal pore enlargement was produced within this pressure range, or alternatively, that any pore enlargement that was achieved was insufficient in and of itself to enhance perfusion of RT PG. As such, 35 kPa vacuum pre-treatment pressure was arbitrarily selected for subsequent perfusion enhancement studies.

Variation of Transmittance with Positive Pressure Post-treatment

Figure 3.6 shows the variation of *NT* with positive post-treatment pressures for microneedled skin treated with RT PG, all 30 min after treatment. Maximum *NT* was observed at 103 kPa for most wavelengths, with up to 41% and 37% improvement relative to untreated skin and RT PG alone, respectively ($P < 0.01$). The decrease of *NT* beyond 103 kPa is likely due to observed PG splashing onto

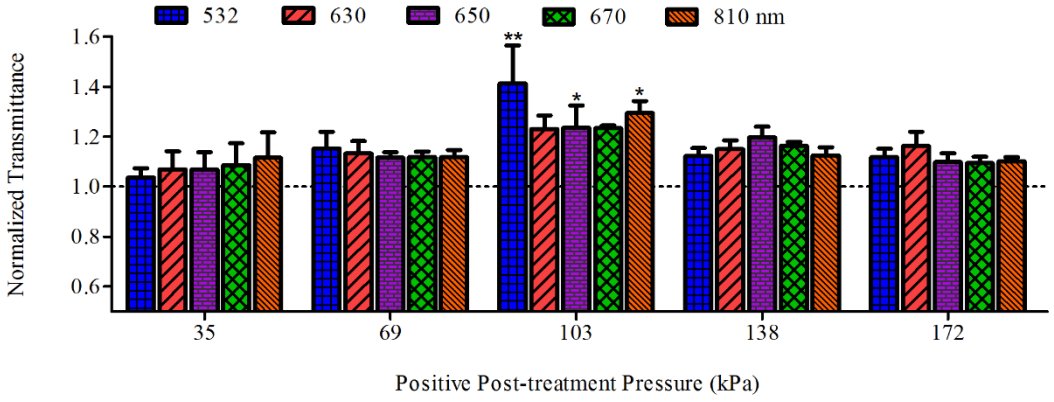

Figure 3.6. Variation of transmittance with positive post-treatment pressures for microneedled skin treated with room temperature PG. Measurements were made 30 min after treatment, and all data are normalized by transmittance for each skin sample before pre-treatment with microneedles (i.e. untreated skin). N = 3 for each condition and error bars represent 1 standard deviation. 2-way ANOVA repeated measures, Bonferroni post-test *$P < 0.05$, **$P < 0.01$, ***$P < 0.001$ relative to 35 kPa.

the sidewalls of the pneumatic apparatus at higher pressures, which may have reduced the amount available for perfusion. Based on this preliminary study, positive post-treatment pressure of 103 kPa was selected for subsequent perfusion enhancement studies.

According to federal Occupational Safety and Health Administration (OSHA), the air pressure threshold that can cause damage if directed at open wounds or body openings is 207 KPa (30 psi) [44] , and the pressure tolerances over muscles and bones in human subjects have been reported in the range of 0.5 - 1.1 MPa [106]. Since the pressures applied in the current study are below these thresholds, pain and damage are not expected in vivo, although further studies in vivo will be required for confirmation. In mechanical tissue optical clearing technique where compression is the only factor in enhancement of light transmission through biological tissue, pressure applied was reported to be 0.13 MPa [90]. However, it is important to note that optical measurements were performed while the skin was pressurized in [27], whereas there was no applied pressure during measurement in the current study. While we presume that positive pressure facilitated tissue clearing by enhancing PG permeation, it is also conceivable that positive pressure enhanced PG solubility in collagen by increasing the PG interactions necessary for tissue clearing [40].

PG Perfusion Enhancement with Combination of Heating, Microneedling, and/or Pneumatic Pressure

Figure 3.7 summarizes the variation of *NT* due to each of the perfusion enhancement techniques individually, as well as in various combinations, all 30 min after treatment. Up to 21% increase in *NT* was observed across most wavelengths after application of RT PG, and there was only modest additional increase with use of 45 ^{o}C heated PG (45 C).

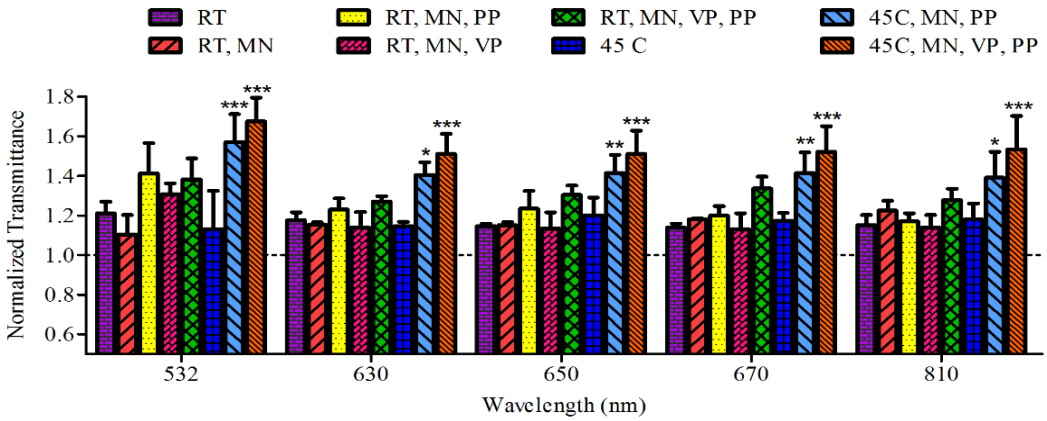

Figure 3.7. Variation of transmittance for skin treated with room-temperature (RT) or 45 °C heated PG (45 C), as well as with various perfusion enhancement techniques, including: pre-treatment with 0.2 mm microneedles (MN); pre-treatment with 35 kPa vacuum pressure (VP); and/or post-treatment with 103 kPa positive pressure (PP). Measurements were made 30 min after treatment, and all data are normalized by transmittance for each skin sample before PG application and/or any perfusion enhancement pre-treatment techniques (i.e. untreated skin). Maximum transmittance was observed with the optimal PG perfusion enhancement protocol shown in the right-most bar at each wavelength, which consisted of heated PG in combination with microneedle and vacuum pre-treatment, followed by positive pressure post-treatment. N = 3 for each condition and error bars represent 1 standard deviation. 2-way ANOVA repeated measures, Bonferroni post-test *P < 0.05, **P < 0.01. ***P < 0.001 relative to RT PG.

This suggests that reduced viscosity was insufficient in and of itself for enhancing PG diffusion through the stratum corneum ($P > 0.05$), as would be expected. The results also demonstrated that use of microneedling pre-treatment (MN), 35 kPa vacuum pre-treatment (VP), and/or 103 kPa positive pressure post-treatment (PP), either separately or combined, lead to only modest enhancement of perfusion of RT PG at most wavelengths ($P > 0.05$). However, the data show that significant increases in *NT* were achieved when these techniques were used in conjunction with heated PG. This suggests that reduced viscosity facilitated the effectiveness of the microneedling and pneumatic pressure perfusion

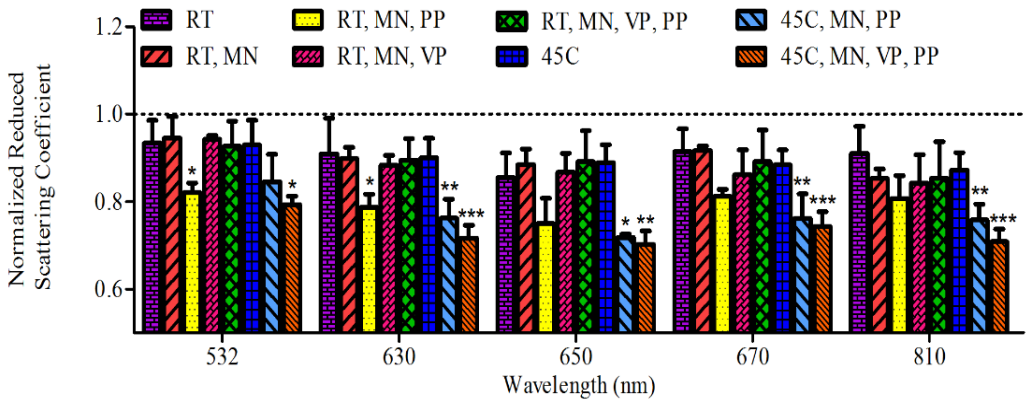

Figure 3.8. Variation of calculated reduced scattering coefficient (μ_s') for skin treated with room-temperature (RT) or 45 °C heated PG (45 C), as well as with various perfusion enhancement techniques, including: pre-treatment with 0.2 mm microneedles (MN); pre-treatment with 35 kPa vacuum pressure (VP); and/or post-treatment with 103 kPa positive pressure (PP). Measurements were made 30 min after treatment, and all data are normalized by reduced scattering coefficient for each skin sample before PG application and/or any perfusion enhancement pre-treatment techniques (i.e. untreated skin). Minimum scattering was observed with the optimal PG perfusion enhancement protocol shown in the right-most bar at each wavelength. N = 3 for each condition and error bars represent 1 standard deviation. 2-way ANOVA repeated measures, Bonferroni post-test *P < 0.05, **P < 0.01, ***P < 0.001 relative to RT PG.

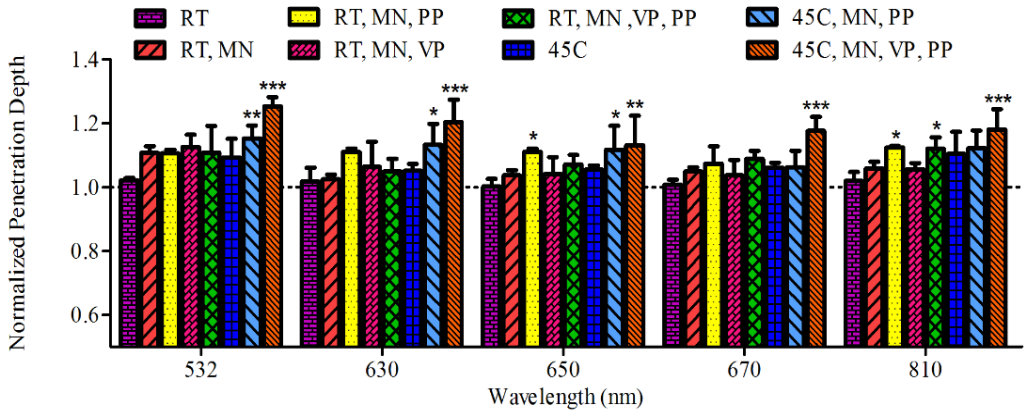

Figure 3.9. Variation of calculated penetration depth (*δ)* for skin treated with room-temperature (RT) or 45 °C heated PG (45 C), as well as with various perfusion enhancement techniques, including: pre-treatment with 0.2 mm microneedles (MN); pre-treatment with 35 kPa vacuum pressure (VP); and/or post-treatment with 103 kPa positive pressure (PP). Measurements were made 30 min after treatment, and all data are normalized by penetration depth for each skin sample before PG application and/or any perfusion enhancement pre-treatment techniques (i.e. untreated skin). Maximum penetration was observed with the optimal PG perfusion enhancement protocol shown in the right-most bar at each wavelength. N = 3 for each condition and error bars represent 1 standard deviation. 2-way ANOVA repeated measures, Bonferroni post-test *P < 0.05, **P < 0.01, ***P < 0.001 relative to RT PG.

enhancement techniques. Finally, for all wavelengths, maximum *NT* was achieved using an optimal PG perfusion enhancement protocol consisting of topical application of 45 °C heated PG in conjunction with microneedle and 35 kPa vacuum pre-treatment, followed by 103 kPa positive pressure post-treatment (*P* < 0.001). Improvements in *NT* up to 68% relative to untreated skin, and up to 46% relative to topical application of RT PG, were observed.

Figures 3.8 and 3.9 show the variation in calculated μ_s' and δ, respectively, due to each of the perfusion enhancement techniques individually, as well as in

various combinations, all 30 min after treatment. Similar to the trends observed for *NT*, μ_s' and δ were only moderately improved with each perfusion enhancement technique individually. However, when used together, in conjunction with heating, up to 30% decrease in μ_s' was observed relative to untreated skin, and up to 20% decrease was observed relative to topical RT PG (at least $P < 0.05$ for all wavelengths). Similarly, up to 25% increase in δ was observed relative to untreated skin, and up to 23% increase was observed relative to topical RT PG (at least $P < 0.05$ for all wavelengths).

Collectively, Figures 3.7, 3.8, and 3.9 demonstrate that significant improvement in clearing can be achieved using the optimal PG perfusion enhancement protocol. It is interesting to note that while the magnitude of clearing varies with laser wavelength, the correlation between wavelength and perfusion condition was not considered significant ($P = 0.8$). Nevertheless, the optimal perfusion condition (45 C, MN, VP, PP) has a definite enhancement trend across all wavelengths, albeit not in the same proportion.

Qualitative Demonstration of Optical Clearing Efficacy

Figure 3.10a shows a schematic illustration of the experimental set up used for demonstration of optical clearing efficacy via thermocavitation. Figure 3.10b shows a sequence of stills captured from high-speed video recording of thermocavitation-induced bubble formation in $CuNO_4$ solution produced during laser fluence through hydrated, *ex vivo* porcine skin treated with the optimal PG

perfusion enhancement protocol. Bubble formation was observed soon after laser turn-on and ceased soon after the laser was turned off. In contrast, no bubble formation was observed when untreated skin was used, and significant thermal damage was observed (data not shown). This demonstrates that well-controlled perfusion of PG within skin can increase the photon density delivered to a specific sub-surface target while minimizing or confining the thermal damage. Determining the effect of less efficient PG perfusion enhancement protocol is beyond the scope of the current study, since the thermocavitation experiments were simply intended

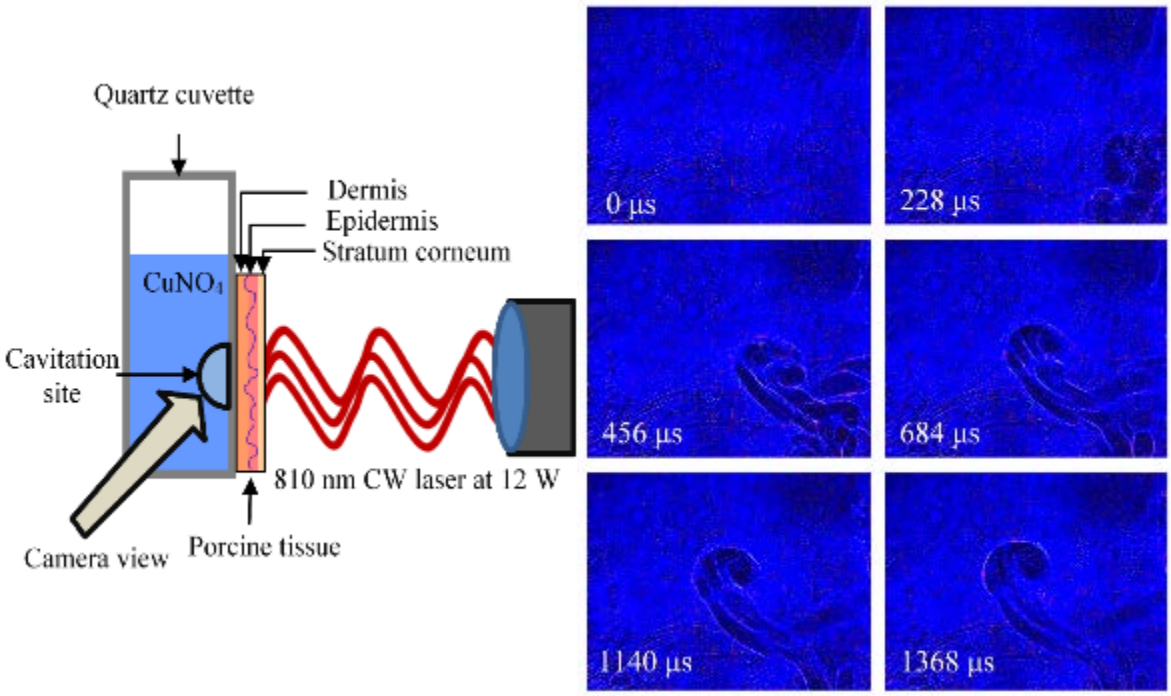

Figure 3.10. Qualitative demonstration of optical clearing efficacy via thermocavitation: a) Schematic illustrating experimental set up; and b) Sequence of stills captured from high-speed video recording of thermocavitation shockwave in aqueous copper nitrate ($CuNO_4$) solution produced during laser fluence through skin treated with optimal PG perfusion enhancement protocol. In similar experiments performed with untreated skin (not shown), bubble formation was not observed, and skin charring occurred.

to serve as a proof-of-concept level demonstration of the enhanced clearing, independent of a particular application.

The current study has provided preliminary evidence supporting the potential afforded by combined microneedling, OCA heating, and pneumatic pressure for enhancing optical clearing performance. However, it important to emphasize that these studies fail to reproduce the full complexity of the *in vivo* environment, and as such, further study is required to determine whether these techniques will yield similar improvements in clinical settings.

Of particular importance in this regard, will be the effect of active perfusion by the vasculature *in vivo*, which may facilitate OCA transport away from the delivery site, and thus, reduce clearing efficacy. Moreover, while no visible skin damage was observed and most of the techniques used in this study have been demonstrated by others to be minimally-invasive on an individual basis, it is unclear whether their use together will be similarly innocuous. Also, future studies need to be performed to examine the effect of various temperature between RT and 45 ^{o}C on the skin and the perfusion of PG. Lower PG is expected to reduce the clearing efficacy, due to increased viscosity of PG. Finally, it is unclear whether the magnitude and depth of clearing that could be achieved *in vivo* using such techniques will be sufficient for all applications. For example, it is conceivable that through-thickness clearing of thin tissues could be achieved using the current techniques (e.g. clearing of scalp for the aforementioned Windows to the Brain

concept). However, for deeper clearing in thicker tissues, it is likely that longer microneedles would be required, which could increase pain and invasiveness.

Conclusions

In this study, we demonstrated, for the first time, the quantitative comparison of a variety of techniques to enhance optical clearing, including microneedling, OCA heating, and pneumatic pressure application. Application of the optimal combination of these techniques on *ex vivo* porcine tissue resulted in 68% increase in *NT* relative to untreated skin, and up to 46% increase relative to topical RT PG application alone. Enhancements in μ_s' and δ were also observed. Collectively, this suggests potential for enhancing optical clearing performance *in vivo*, and thus, potential for facilitating the use of medical lasers in numerous clinical applications.

Acknowledgments

I would like to acknowledge the contribution of my co-authors to this study: Bissrat Melakeberhan, Dr. Masaru P. Rao and Dr. Guillermo Aguilar. I would like to acknowledge the American Society for Lasers in Medicine and Surgery (ASLMS) for a travel grant awarded to YD to present research leading to this study at the 33rd Annual ASLMS Conference, Boston, MA, April 2013. Additionally, I thank Mr. Earl Steward, Lab Director in Department of Surgery, University of California Irvine, School of Medicine, for providing the porcine tissue. I also acknowledge Mr. Roberto Ayala for his contribution to data

collection, Mr. Darren Banks for his contribution to thermocavitation studies, and Dr. Omid Khandan for his contribution to microneedle poration characterization.

Chapter 4. Inflammatory Response to Implantation of Transparent Nanocrystalline Yttria-Stabilized Zirconia using a Dorsal Window Chamber Model

Introduction

Craniotomy is an established procedure in neurosurgery to decrease intracranial pressure after brain infarction, intracranial hemorrhage, and brain traumatic injury resulting from cerebral edema. During this procedure parts of the brain become exposed, leaving it unprotected and giving the patient a malformed appearance. Cranioplasty is the subsequent surgical procedure to restore the aesthetic appearance of the cranium and provide the necessary mechanical protection to the brain.

A successful cranioplasty has shown to improve electroencephalographic abnormalities, cerebral blood flow abnormalities, and other neurological abnormalities [107-109]. . The ideal material used for cranioplasty needs to be 1) radiolucent , 2) resistant to infections, 3) thermal insulator, 4) resistant to mechanical load, 5) malleable to fit defects with complete closure, and ideally, 6) inexpensive [110]. Over time, a broad spectrum of synthetic materials have been used for cranioplasty [111], including titanium and PEEK (poly-ether-ether ketone) [112, 113]. A new thermoplastic matrix system PEKK (poly-ether-ketone-ketone), resembles bone more so than titanium [114, 115]. PEEK and PEKK are more elastic and are less dense which pose some advantages, whereas titanium has a

higher yield and ultimate strength, making it mechanically more stable [116]. PEKK has higher compressive strength than PEEK and has demonstrated to have superior performance in mechanical properties, fracture toughness and damage tolerance [117, 118].

All these materials seem appropriate to protect the brain against mechanical trauma. However, these polymers do not provide the requisite combination of properties required for clinically-viable transparent implants. During the past few years, researchers have been working on several promising options to circumvent the limitations of current materials for cranial reconstruction [111]. Our own group has aimed at and developed a novel transparent ceramic material capable of providing access to the brain for imaging or therapeutic purposes [45]. This material is nanocrystalline yttria-stabilized-zirconia (nc-YSZ), and it is synthesized by a relatively new densification process known as current activated pressure assisted densification (CAPAD) technique [65, 119]. YSZ produced using conventional ceramic processing methods is typically opaque, due to scattering induced by micrometer-scale (and larger) internal porosity [37]. CAPAD technique enables reduction of internal porosity to nanometric dimensions. At this length scale, porosity is sufficiently small to minimize scattering in the spectral range of interest for laser-based diagnostics and therapeutics [37].

We envision nc-YSZ implants providing an exquisite combination of transparency and toughness for clinically-viable transparent cranial implants [33,

116]. In the long term, we expect these implants to be suitable for chronic optical access to the brain, necessary for optical imaging, optogenetics, photodynamic therapy, low-level-laser therapy as well as other neuroscience and neuroengineering applications [45].

In addition to their transparency and mechanical toughness, these materials should be biocompatible and support angiogenesis and neovascularization. While angiogenesis is mainly characterized by the protrusion and outgrowth of capillary buds and sprouts from pre-existing blood vessels, neovascularization comprises the formation of functional microvascular networks with red blood cell (RBC) perfusion [120]. Of interest, both processes are required to ensure successful engraftment of the construct into the surrounding host tissue. To exhibit an adequate biocompatibility, these materials should not induce a severe local or systemic inflammatory reaction.

The interaction of implanted biomaterials with the host tissue is a dynamic process, which is subsumed under the term ‘foreign body reaction’ and comprises distinct steps [121]. Immediately after implantation into the body, a layer of proteins forms onto the surface of the implant, which critically influences the subsequent cellular reaction to the implant [122, 123]. This reaction is characterized by the activation of leukocytes, which infiltrate the implantation site and produce various cytokines and growth factors [124]. Moreover, monocytes are recruited from the blood stream and start to differentiate into macrophages [125]. The inflammation

can result in chronic foreign body reaction, which is associated with the accumulation of lymphocytes and fusion of individual macrophages to multinucleated giant cells, which are typically found at the interface between the implanted biomaterial and the surrounding host tissue [126]. Lastly, there is fibroblast proliferation and migration, as well as neovascularization or fibrous encapsulation around the implant. Because a foreign body reaction involves a broad range of different cell types, cytokines and growth factors, it is impossible to simulate adequately this complex process in vitro, and in vivo analysis remain fundamental for the successful evaluation.

The dorsal window chamber model (DWCM) is an in vivo microvascular tissue model that allows the study of the intact microcirculation by the means of intravital microscopy using transillumination and without the use of fluorescence molecules [127], thus, limiting light toxicity and allowing for the study of microvascular changes over long periods of time (up to 60 days). This chronic model has been broadly used during the last three decades for repetitive in vivo analysis of the microcirculation, tumor biology and for study of biomaterials [127-129]. It has provided deep insights into the mechanisms regulating the hemodynamic, angiogenic, and inflammatory response to implanted biomaterials [127, 128]. Specifically, this model has been used to study the host tissue response to cranioplasty biomaterials such as ceramic calcium phosphate compounds [130, 131] and titanium [132-134].

Nc-YSZ is expected to be placed on intact dura to replace the bone flap that is injured or removed during cranioplasty; therefore, it would be in direct contact with soft tissue at the implant site. Therefore, implantation of the Nc-YSZ in the DWCM can allow us to study the effect of the implantation in the microvasculature in vivo. Traditional opaque YSZ has proven biocompatibility in dental and orthopedic applications [33], while information about the biocompatibility of the transparent nc-YSZ is lacking.

Our objective in this study is to use the DWCM to quantify the inflammatory and hemodynamic changes at the microscopic level resulting from implantation of nc-YSZ. To our knowledge, no model has been used which permits the direct observation of the dynamic process of the host to compare the nc-YSZ, PEEK and PEKK. Our study is focused on the continuous in vivo analysis of microcirculatory parameters of the host tissue in response to biomaterial implantation. We hypothesize that the stability and mechanical characteristic of nc-YSZ will show similar or lower cellular response than PEEK and PEKK, and that the inflammatory response to the surrounding soft tissue is associated with micro-hemodynamics and vascular permeability changes normal to any implant.

Materials and Methods

Animal Model

Animal handling and care were provided following the Care and Use of Laboratory Animals [135]. All animal experiments were conducted under a protocol approved by the University of California, San Diego Institutional Animal Care and Use Committee. Male Golden Syrian hamsters of 50-70 g were fitted with a one-sided window chamber consisting of two titanium supports, one of which holds a 12-mm-diameter glass window. The complete surgical technique was reported previously [136, 137]. Briefly, the animals were prepared for chamber implantation with a 50 mg/kg i.p. sodium pentobarbital anesthesia [136]. After hair removal, two sutures were used to lift the dorsal skin of the back away from the animal and one frame of the chamber was positioned on the animal's back. With the aid of backlighting and a stereomicroscope, following the outline of the window, skin was removed until only a thin monolayer of retractor muscle and the intact subcutaneous skin of the opposing side remained.

Implantation

A small square of 2 by 2 mm with a thickness of 100 μm were cut and sterilized prior implantation. Nc-YSZ (fabricated by current activated pressure assisted densification (CAPAD) technique [119]), PEEK (McMaster-Carr, Los Angeles, CA), and PEKK (Oxford Performance Materials, South Windsor, CT)

were placed directly onto the striated muscle and subcutaneous tissue under the cover slip (Figure 4.1). During implantation a drop of saline solution was used to hold the sample in place between the exposed skin and the frame of the chamber.

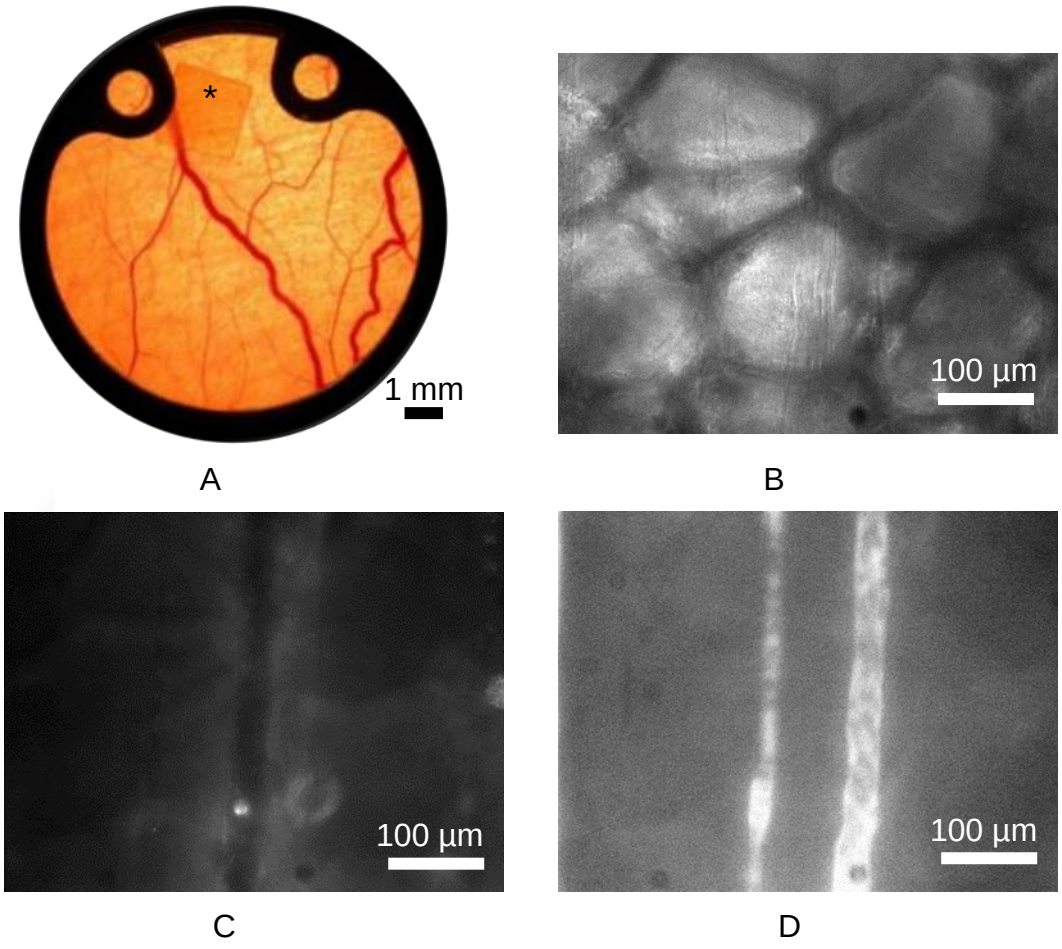

Figure 4.1. (A) Photograph of dorsal skinfold chamber of syrian golden hamsters, containing striated muscle and skin and allowing for repeated analysis of the microcirculation in the awake hamster for two weeks. Here a nc-YSZ sample (*) was implanted. (B, C, D) Representative intravital Fluorescence Microscopy image of the microcirculation under the nc-YSZ implant 15 days after implantation at 20x with: (B) White light; (C) Green-light epi-illumination upon injection of Rhodamine 6G for direct labeling of activated leukocytes. (D) Blue-light epi-illumination upon injection of macromolecular fluorescent dye FITC-labeled Dextran.

Stainless steel nuts were used as spacers to separate the frames 450 to 500 μm. The animal was allowed to rest for 2 days, at which time its chamber was evaluated under the microscope (650x) for any sign of infection, edema, or bleeding. Animals absent of any microvascular complication were anesthetized again with sodium pentobarbital and implanted with arterial and venous catheters (PE-50) in the carotid artery and jugular vein, respectively. The arterial catheter was initially filled with heparinized saline (40 IU/ml), to ensure patency of the catheter for the entire length of the experiment. These catheters were tunneled under the skin and exteriorized at the dorsal side of the neck where they were attached to the chamber frame with tape.

Inclusion Criteria

Hamsters were suitable for the experiments if: 1) systemic parameters were within normal range. Namely, heart rate (HR) > 350 beat/min, mean arterial blood pressure (MAP) > 80 mmHg, systemic hematocrit (Hct) > 45%, and arterial PO_2 pressure (PaO_2) > 50 mmHg; and 2) microscopic examination of the tissue in the chamber observed under x650 magnification did not reveal signs of edema or bleeding. Hamsters are fossorial animals with a low arterial PO_2 compared to other rodents; however, the PO_2s in the window chamber are similar to the PO_2s in other rodents [138].

Experimental Groups

Animal were assigned randomly to the different experimental groups. Groups are labeled based on the material implanted. Accordingly, this study includes four experimental groups: 1) **Control** (*n* = 3, without any implant); 2) **Nc-YSZ** (*n* = 7); **PEEK** (*n* = 4); and **PEKK** (*n* = 4).

Intravital Microscopy Experimental Setup

The animals were restrained in a tube and the protruding window chamber was fixed to the microscopic stage for transillumination (BX51WI, Olympus, New Hyde Park, NY). Measurements were carried out using a 40X (LUMPFL-WIR, numerical aperture 0.8, Olympus) water immersion objective. Animals were given 10 to 15 min to adjust to the tube environment before any measurement. Detailed mappings were made of the chamber vasculature so that the same vessels studied at baseline could be followed throughout the experiment. Blood vessels were chosen by a distinctive anatomic landmark to easily and quickly reestablish the same fields and vessels at each observation time point. Tissue was transilluminated with a mercury arc lamp (100 W, Walker Instruments, Scottsdale, AZ) and a 400 nm interference filter (Spectra Physics, no. 59820). Images were recorded with a high speed video camera (1000 x 1000 pixels, 2000 frames per second, Fastcam 1024 PCI, Photron, San Diego, USA). Camera shutter speed was 1/10 of frame rate.

Microhemodynamics

A video image-shearing method was used to measure vessel diameter (D) [139]. Changes in arteriolar and venular diameter from baseline were used as indicators of a change in vascular tone. Arteriolar and venular centerline velocities were measured off-line using the image cross-correlation method [140]. The measured centerline velocity (V) was corrected according to vessel size to obtain the mean RBC velocity [141]. Blood flow (Q) was calculated from the measured values as $Q = \pi \times V (D/2)^2$.

Leukocyte Endothelial Interaction

To label leukocytes, animals received intravenous injection of 5 mg/kg of Rhodamine 6G (Sigma-aldrich, St Louis) infused in a volume equal to 0.1 mL. Fluorescently labeled leukocytes were excited and images were captured with a Vivid Set (XF104-2 filter, Omega Filters, Brattleboro, VT) using a low light camera (ORCA 9247, Hamamatsu, Tokyo, Japan). Briefly, a straight portion of blood vessels was illuminated for 60 sec and video was recorded (10 frames/s). Leukocytes were counted during video playback in a 100 μm length segment and categorized according to their flow behaviour as “free-flowing”, “rolling” on the endothelium, and “immobilized” cells [142]. The rolling leukocytes were white cells rolling on the endothelium and reported as the percentage of all leukocytes passing, “free-flowing”.

Macromolecule Vascular Permeability

Vascular permeability was study after intravenous injection of 5mg/kg fluorescein isothiocianate (FITC) conjugated dextran with a molecular weight of 150 kDa (FITC-dextran) infused in a volume equal to 0.1 mL. Fluorescent macromolecular permeability was studied by measuring the fluorescence intensities of the perivascular and intravascular space for the blood vessels studied. FITC-dextran fluorescence were excited and images were captured with a Vivid Set (XF25 filter, Omega Filters, Brattleboro, VT) using a low light camera (ORCA 9247, Hamamatsu, Tokyo, Japan). Fluorescence levels were measured using ImageJ (Java-based image processing program developed at the NIH by Wayne Rasband, http://rsb. info. nih. gov/ij/). Intensities of the perivascular space directly adjacent to the blood vessel wall (E_1) and intensity of the intravascular space (E_2), were used to estimate a extravasation index (E), defined as $E=E_1/E_2$.

Microvascular Experimental Protocol

Awake animals were restrained in a plexiglas tube from which the window chamber protruded, the restraining tube was fixed to the intravital microscope stage. Hemodynamic measurements were made 2, 5, 7, 10, 12 and 15 days after material implantation. Leukocyte endothelia interaction and macromolecule vascular permeability were studied 15 days after material implantation. Microhemodynamics, leukocyte-endothelial interaction, and macromolecule permeability were assessed in different microvascular regions of interest (ROI)

including issue behind the implant, tissue surrounding the implant, tissue far away from the implant. In each ROI, six to eight arterioles and venules were selected in each preparation. Fields of observation and vessels were chosen for study at locations in the tissue where the vessels were in sharp focus. After 15 days, animals were euthanized.

Statistical Analysis

Results are presented as mean ± standard error of the mean (SEM). Hemodynamic results within each group were analyzed using analysis of variance for repeated measurements (ANOVA, Kruskal-Wallis test). When appropriate, post hoc analyses were performed with the Dunn's multiple comparison test. Hemodynamic data comparison between groups was analyzed using two-way analysis of variance (Two-way ANOVA test). When appropriate, post-test analyses were performed with the Bonferroni post-tests comparison. Leukocytes adherent and rolling, and vascular permeability of each groups were tested for normality according to the Shapiro-Wilk test, and analyzed using analysis of variance for repeated measurements (ANOVA, Brown-Forsythe test). When appropriate, post hoc analyses were performed with the Bonferroni's multiple comparisons test. Microhemodynamic data is presented normalized to day 2 after implantation. All statistics were calculated using GraphPad Prism 5.01 (GraphPad Software, Inc., San Diego, CA). Changes were considered statistically significant if $P < 0.05$.

Results

All animals completed the study protocol without visible sign of discomfort. Animals were observed resting and periodically eating throughout the experiment. In Figures 4.2 – 4.4, Week 1 consisted of data collected on days 5 and 7, and Week 2 consisted of data collected on days 10, 12, and 15.

Microhemodynamics: Microvascular Diameter

Diameter of a total number of 45 arterioles was investigated (control, *n* = 8; nc-YSZ, *n* = 20, PEEK, *n* = 8, PEKK, *n* = 9). Range of inner diameter of baseline arterioles proved to be similar in all groups (control, 34-68 µm; nc-YSZ, 36-84 µm; PEEK, 39-68 µm; PEKK, 24-70 µm). No statistically significant difference was observed in microvascular variables measured at day 2 between groups. The results in Figure 4.2A indicated that the mean arterioles in animals in all four groups exhibited slight vasodilation over two weeks (mean > 1). However, the vasodilation was not statistically significant for implants in comparison with control in each week.

Diameter of a total number of 52 venules was investigated (control, *n* = 12; nc-YSZ, *n* = 21; PEEK, *n* = 10; PEKK, *n* = 9). Range of baseline venules was similar in all groups (control, 28-68 µm; nc-YSZ, 27-84 µm; PEEK, 32-68 µm;

PEKK, 35-70 µm). The results in Figure 4.2B reveals almost constant venular diameters over time, with minor difference between the groups.

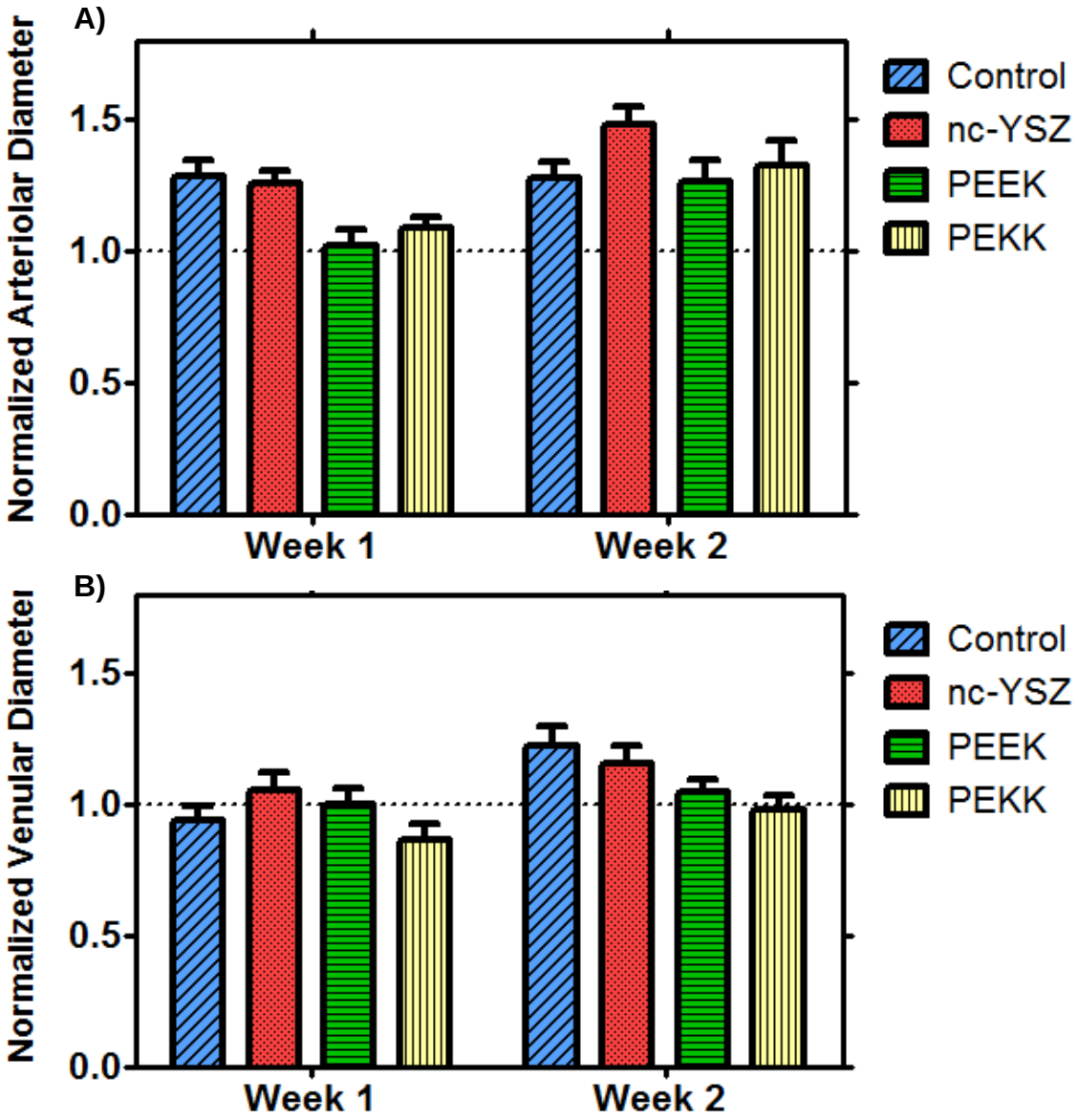

Figure 4.2. Normalized arteriolar (A) and venular (B) diameter of dorsal skinfold chamber of hamsters implanted with nc-YSZ, PEEK and PEKK in comparison with control (no implant). 2-way ANOVA repeated measures, Bonferroni post-test *P < 0.05, **P < 0.01, ***P < 0.001 relative to control.

Microhemodynamics: Microvascular Velocity

The computed velocity profiles characterized by the velocity of RBC and obtained from in vivo videos depict a parabolic shape based on a Newtonian fluid

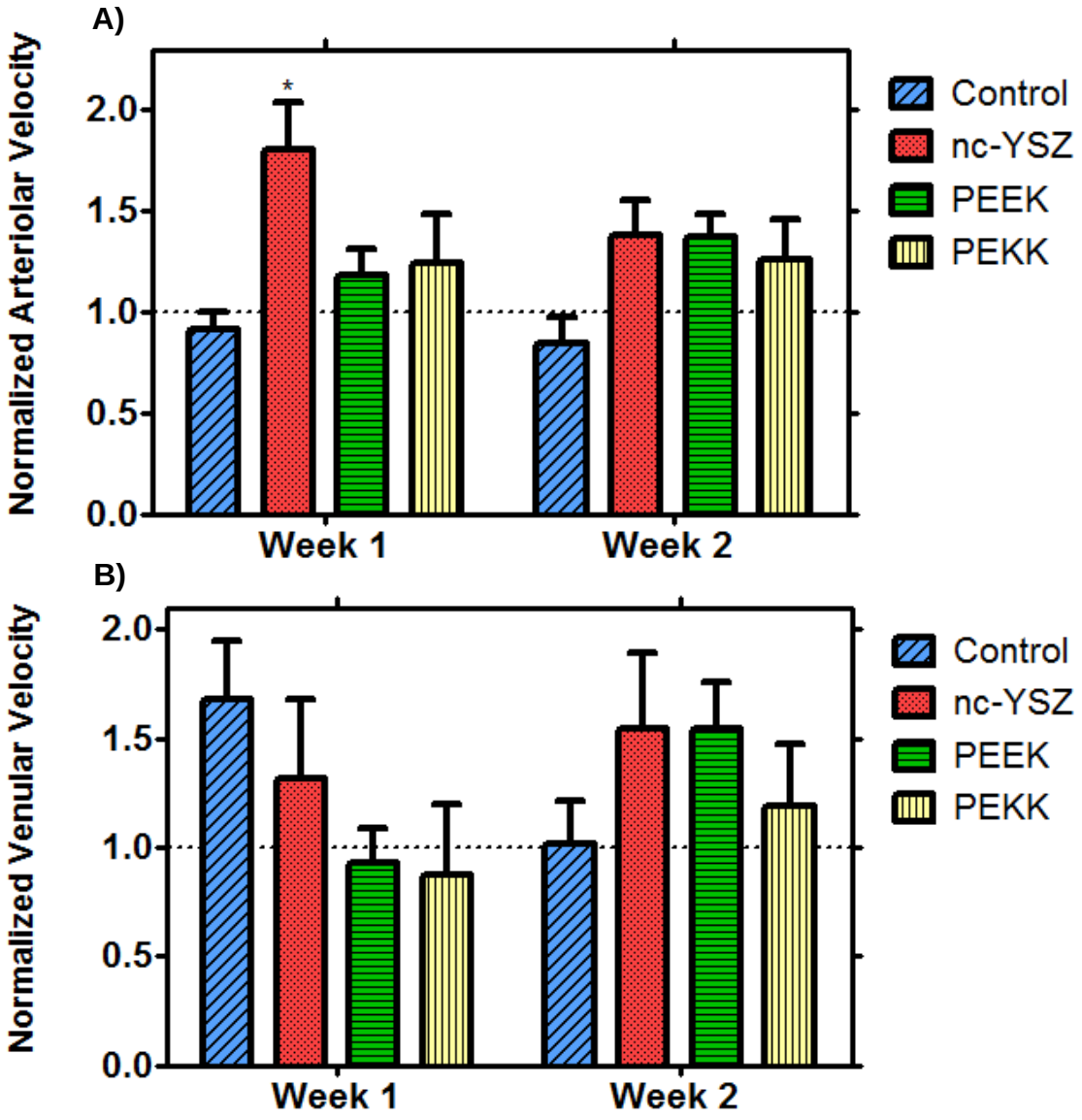

Figure 4.3. Normalized arteriolar (A) and venular (B) velocity of dorsal skinfold chamber of hamsters implanted with nc-YSZ, PEEK and PEKK in comparison with control (no implant). 2-way ANOVA repeated measures, Bonferroni post-test *P < 0.05 relative to control.

laminar flow assumption. Velocity of a total of 39 arterioles was investigated for two weeks (control, *n* = 20; nc-YSZ, *n* = 7; PEEK, *n* = 6; PEKK, *n* = 6). Range of baseline arteriolar velocity was similar in all groups (control, 0.31-3.95 mm/s; nc-YSZ, 1.58-5.12 mm/s; PEEK, 0.96-2.65 mm/s; PEKK, 0.72-3.29 mm/s). Figure 4.3A shows that the implantation of nc-YSZ seems to initially evoke a statistically significant increase in arteriolar velocity in comparison with control. However, the arteriolar velocity declined in the second week and reached a value comparable to control, PEEK, and PEKK.

Velocity of a total of 46 venules was investigated for two weeks (control, *n* = 15; nc-YSZ, *n* = 14; PEEK, *n* = 7; PEKK, *n* = 10). Range of baseline venular velocity was similar in all groups (control, 0.49-5.04 mm/s; nc-YSZ, 0.31-4.21 mm/s; PEEK, 0.12-3.51 mm/s; PEKK, 0.12-0.72 mm/s). Figure 4.3B shows that during the first week, the venular velocity for animals with PEEK and PEKK was decreased while it increased for control and nc-YSZ. However, the difference in the venular velocity of all groups during two weeks was not statistically significant.

Microhemodynamics: Microvascular Flow

Figure 4.4 reveals that the changes in arteriolar and venular flow in animals of all groups were not statistical significant. The slight increase in arteriolar flow over time is due to anatomical changes and vasodilation over two weeks. Therefore, data indicated that the microvascular blood flow of animals was not impaired by implantation of the materials.

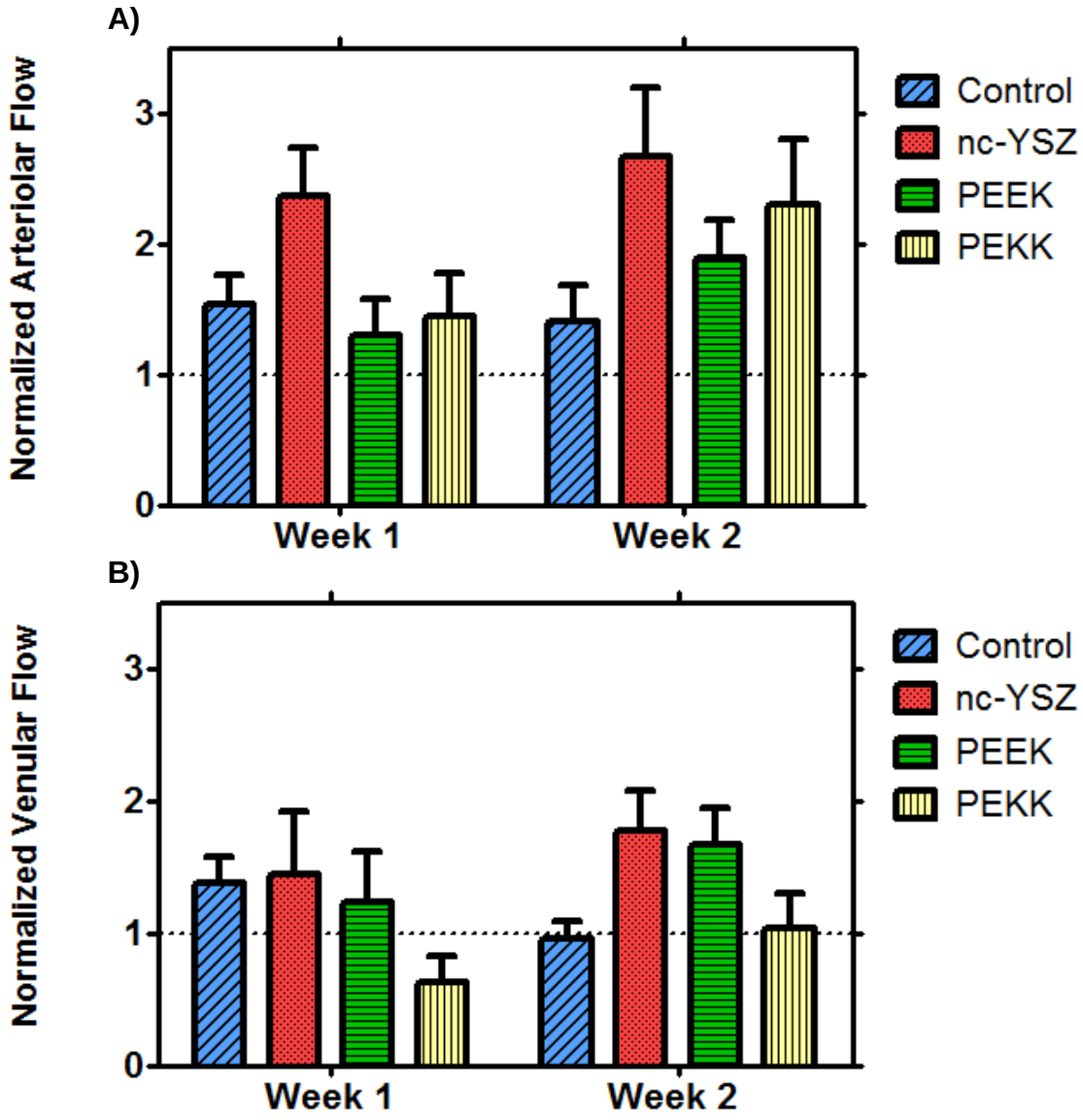

Figure 4.4. Normalized arteriolar (A) and venular (B) flow of dorsal skinfold chamber of hamsters implanted with nc-YSZ, PEEK and PEKK in comparison with control (no implant). 2-way ANOVA repeated measures, Bonferroni post-test *P < 0.05, **P < 0.01, ***P < 0.001 relative to control.

Inflammation: Leukocyte-endothelial Cell Interaction

In each group, 30 venules were analyzed after two weeks. Figure 4.5 demonstrated that nc-YSZ only induced a transient change in leukocyte

endothelial cell interactions in venules of the host tissue (17%) in comparison with the control (19%) after the first 15 days of implantation, indicating a high degree of biocompatibility. The lack of an inflammatory reaction to implants (no statistical significance) indicated an adequate biocompatibility of nc-YSZ comparable to that of PEEK, PEKK and control hamsters.

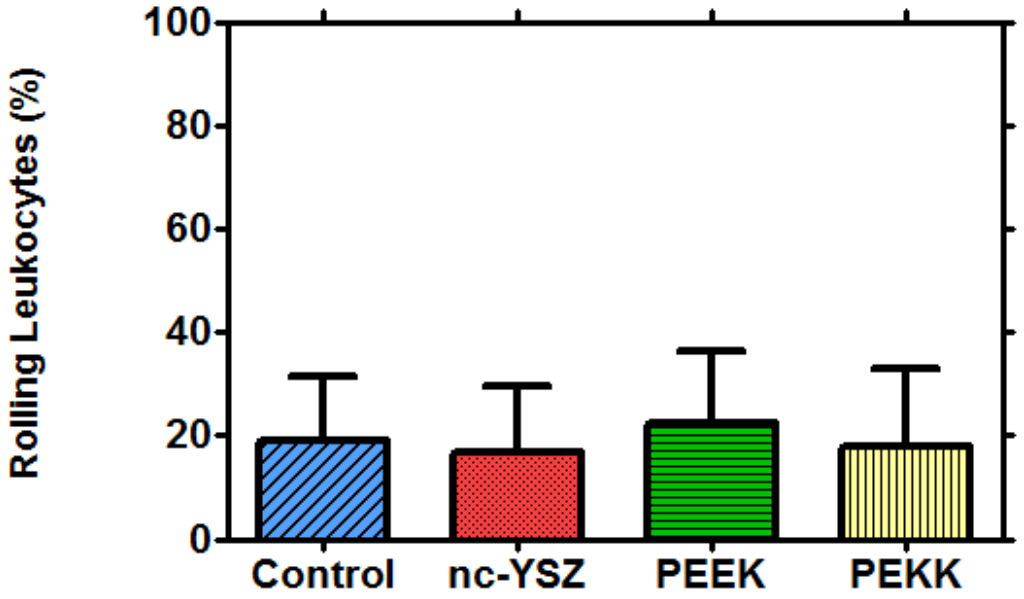

Figure 4.5. Number of rolling leukocytes (given in % of non-adherent leukocytes) in venules of hamster dorsal skinfold 15 days after control (no implant) and implantation of nc-YSZ, PEEK, PEKK. N = 20 for each condition and error bars represent 1 standard deviation. 2-way ANOVA repeated measures, Bonferroni post-test *P < 0.05 relative to control.

Microvascular Permeability

The macromolecular leakage was increased for all implant groups with no statistical significance (Figure 4.6). For all groups, the macromolecular leakage

values were below 0.8-1, an intact endothelial integrity can be assumed [143]. Therefore, nc-YSZ did not increase vascular permeability when compared to control and commercial implants.

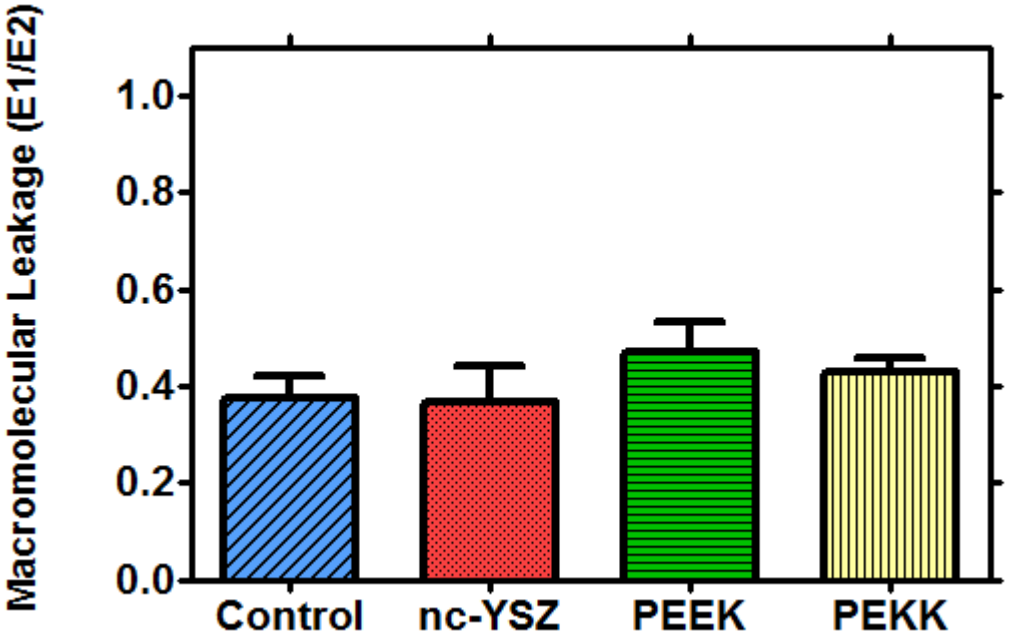

Figure 4.6. Macromolecule leakage as an indicator of microvascular permeability in venules of striated muscle in hamster dorsal skinfold 15 days after control (no implant) and implantation of nc-YSZ, PEEK, PEKK. N = 20 for each condition and error bars represent 1 standard deviation. 2-way ANOVA repeated measures, Bonferroni post-test *P < 0.05, **P < 0.01, ***P < 0.001 relative to control.

Discussion

In this report, the DWCM was used to study the microcirculation by means of intravital microscopy using transillumination. Previously, this model proved to be ideal for the systematic in vivo analysis of the host tissue interaction with

biomaterials [133, 144, 145]. Specifically, this model has been used to study the host tissue response to cranioplasty biomaterials such as ceramic calcium phosphate compounds [130, 131] and titanium [132-134].

Conventionally-processed microcrystalline YSZ (mc-YSZ) has well-proven biocompatibility in dental and orthopedic applications [33]. However, biocompatibility assessments for nc-YSZ specifically are necessitated by the unique properties associated with nanocrystallinity (e.g. increased surface energy). The prolonged inflammatory response to an implant is one of the primary causes for the failure to integrate into tissue [111].

Figure 4.2 demonstrated that changes in arteriolar and venular diameter in hamsters with nc-YSZ implant were not significantly different than those of control and commercially available implants (PEEK and PEKK). Significant vasodilation in the dorsal skinfold chamber of hamsters would be an initial sign of infection or acute inflammation [144]. Figure 4.3 revealed a statistically significant increase in the arteriolar velocity of hamsters with nc-YSZ implants in comparison with control in week 1. However, by week 2, this difference decreased and became insignificant. Figure 4.4 shows insignificant difference between the microvascular blood flow of all groups, indicating that implants did not disturb the blood flow.

Analysis of microvascular permeability by quantifying the extravasation of macromolecules, shown in Figure 4.6, indicated that the endothelial lining of postcapillary and collecting venules were not damaged as a result of nc-YSZ

implantation. Additionally, we have demonstrated the lack of activated leukocytes in venules for all groups, indicating that the nc-YSZ, PEEK, and PEKK did not induce an acute inflammatory response in the host tissue. Thus, nc-YSZ exhibited a good biocompatibility that was comparable to that of control, PEEK and PEKK.

While PEEK and PEKK are FDA-approved commercially available cranial implants, this is the first study, to the best of our knowledge, to observe microhemodynamics changes in a hamster backflap model in response to PEEK and PEKK implants. One limitation of using the dorsal skinfold chamber model to study biomaterial reaction is that this model cannot directly predict the bone ingrowth and response around the implant. Comprehensive characterization of nc-YSZ as a cranial material should be performed by combining the results of this study with other models such as calvarial defect model [146].

In summary, this study demonstrated that nc-YSZ does not impair microcirculation and endothelial integrity of striated muscle in the hamster dorsal skinfold model. The nc-YSZ also did not result in enhanced leukocyte activation and was as equally tissue-compatible as commercial PEEK and PEKK cranioplasty materials. Clinically, the results presented in this report indicate that nc-YSZ may represent a good alternative for cranial implants.

Acknowledgments

I would like to acknowledge the contribution of my co-authors to this work: Diego E Galan-Hoffman, Daniel Ortiz, Dr. Pedro Cabrales and Dr. Guillermo

Aguilar. Also, I would like to acknowledge the American Society for Lasers in Medicine and Surgery (ASLMS) Student Research Grant awarded to YD to conduct this study and for the travel grant awarded to YD to present research leading to this study at the 34th Annual ASLMS Conference, Phoenix, AZ in April 2014. I also thank Dr. Javier Garay and Dr. Yasuhiro Kodera for providing the nc-YSZ sample.

Chapter 5. Evaluation of Laser Bacterial Anti-Fouling of Transparent Nanocrystalline Yttria-Stabilized-Zirconia Cranial Implant

Introduction

The fundamental aim of the Window to the Brain (WttB) implant/platform is to improve patient care by providing a technique for delivery and/or collection of light into/from the brain, on demand, over large areas, and on a chronically-recurring basis without the need for repeated craniotomies. Transparent nanocrystalline yttria-stabilized-zirconia (nc-YSZ) provides transparency and toughness required for enhancing the light-based diagnosis and treatment of a wide variety of brain pathologies including cerebral edema, traumatic brain injury, stroke, glioma, and neurodegenerative diseases, among many others. Using optical coherence tomography (OCT), we demonstrated the initial feasibility of nc-YSZ cranial implants within the context of cortical imaging of an acute murine model [45]. For optical clearing of the scalp temporarily, our study on delivery techniques of optical clearing agents (OCA) showed that the combination of heated propylene glycol (PG), microneedling and vacuum pre-treatments, and positive pressure-post treatment significantly enhanced the perfusion of topically applied PG [44].

Unfortunately, bacterial adhesion to cranial implant biomaterials (fouling) is followed by colonization, biofilm formation, infection and, eventually, implant failure [147, 148]. Despite advances in sterilization and antiseptic techniques, deep

infection is the major leading complication after cranioplasty, with reported rates between 21% and 40% [149-152]. Infection might evolve due to contamination during surgery, local infections elsewhere in the body, or suppressed immune system [148]. Thus, bacterial adhesion to the implant and biofilm formation may limit the use of WttB for optical imaging and therapy, especially in immunocompromised patients. In particular, Escherichia coli (E. coli) is one of the most common isolates in gram-negative bacillary meningitis after cranial surgery or trauma in adults [147, 153]. It has also been shown that E. coli peritonitis causes increased blood-brain barrier permeability [154]. Due to poor penetration of antimicrobial agents to the cerebrospinal fluid and resistance of biofilms to antimicrobial agents, the conventional treatment for cranial implant infection is removal and replacement of the implant, adding delays and cost to cranioplasty [155, 156].

Sterilization of implant surfaces using lasers has been suggested [157, 158] and resulted in several promising reports [159, 160]. Previous data, however, demonstrates that temperature increase of 10 ^{o}C induces tissue damage in the bone [161-163] and denaturation of lipids and proteins [164]. It is critical, therefore, to ensure that the temperature stays below the threshold for thermal damage during laser application.

Genetically engineered bacteria that emit bioluminescence has been used in several models to optically monitor bacterial number and viability in real time

[165]. Bioluminescent bacteria only produce light when they are alive and metabolically active because bacterial luciferase is an energy-requiring oxygenase [166]. Validation of a non-invasive, real-time imaging technology using bioluminescent E. coli has been validated in the neutropenic mouse thigh model of infection [167]. This technique shows that the intensity of luminescence images is proportional to the magnitude of the infection.

The transparency of the nc-YSZ implant provides us with the unique opportunity to shine a near-infrared (NIR) laser to treat the infected biomaterial locally and chronically, on-demand, without the need for removing the implant. Although the use of lasers to reduce bacterial growth in vitro was previously reported [168-170], their use for non-invasive treatment is entirely novel. This in vitro study monitors bacterial growth while monitoring the temperature to optimize laser irradiation parameters. Herein, we investigate the efficacy and the governing mechanism of the CW and PW NIR laser for disruption of the biofilm under the nc-YSZ implant in vitro.

Materials and Methods

Implant Fabrication and Preparation

Transparent nc-YSZ cranial implants were fabricated with current activated pressure assisted densification (CAPAD) technique, an emerging technique that enables reduction of internal porosity to nanometric dimensions, and thus,

reduction of the optical scattering that renders typical YSZ opaque [65]. Details of nc-YSZ fabrication and optical characterization have been reported previously [37, 119]. The average surface roughness (Ra) of the nc-YSZ samples used in this study was measured using atomic force microscopy (AIST-NT) to be approximately 10 nm. Prior to each experiment, nc-YSZ samples were dry sterilized (Germinator 500) at 250 ^{o}C for 10 seconds to remove all preexisting bacteria.

Bacteria Inoculation

For all experiments, genetically engineered BL21 Escherichia Coli (CMC0014, Sigma Aldrich) phenotype that emits bioluminescence was used. Briefly, BL21 cells were transformed with *P. Pyralis* luciferase gene using pet28 vector. The transformants were cultured in Lysogeny Broth (LB) media supplemented with Kanamycin antibiotic (K+). Laser irradiation experiments were run on agar plates containing K+ and protein expression inducer Isopropyl β-D-1-thiogalactopyranoside (IPTG). Specifically, BL21 E. coli culture was grown overnight in the shaker at 37˚C or 16 hours in the K+-LB until the OD_{600} reached 0.6-0.7. One (1) µL of the overnight culture was diluted in 100 µL of fresh K+-LB media. As shown in Figure 5.1, agar plates were placed on a heated pad set to body-temperature. For each experiment, 0.5 µL of the diluted bacteria was placed

on agar and the nc-YSZ was placed on top. The bacteria underlying nc-YSZ was then treated with selected laser parameters and incubated for 24 hours.

Bioluminescence Imaging System

Each sample was imaged 24 hours after laser irradiation. Prior to bioluminescence imaging, 100 µL of the luciferase substrate (D-Luciferin, potassium salt 150 µg/ml, Research Products International Corp.) was added at room temperature to evenly cover each sample. Light emission of the bioluminescent bacteria was detected using a Macro Luminescence Dark Box (Stanford Photonics, Inc, Palo Alto, CA). Two images were taken of each sample. The first image was a grayscale image with 0.2 sec exposure of the plate illuminated by halogen white light located atop the imaging chamber. The second image was a 5 sec exposure at 2 MHz rate of the sample taken in darkness to measure low-level bioluminescent emission. ImageJ software (National Institute of

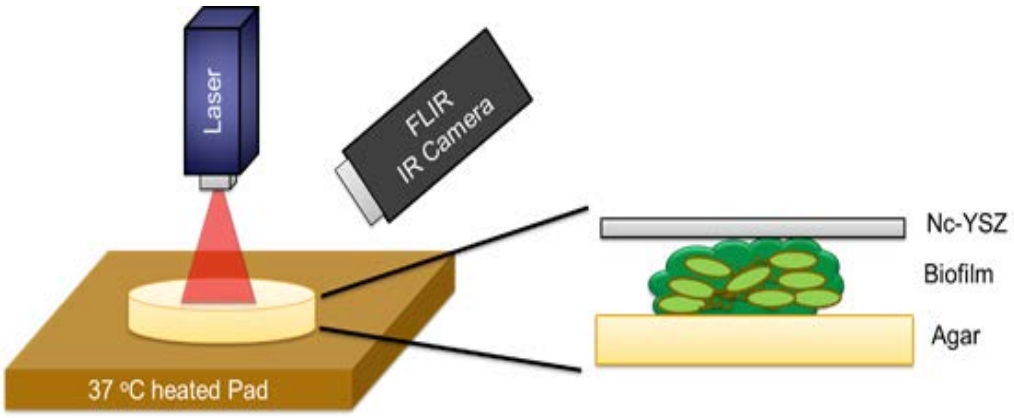

Figure 5.1. (a) Schematic diagram for the treatment of biofilm under nc-YSZ with NIR laser irradiation. (b) Cross sectional view of the set up.

Health) was used to quantify the light emission at the irradiated Regions of Interest (ROIs). The ROIs encompassed a circle equal to the beam diameter of 4 mm ($1/e^2$). The relative luminescence unit (RLU) in the ROI was normalized relative to the RLU outside of the ROI for each sample. The imaging procedure, acquisition parameters, and post-analysis were kept constant for all measurements.

Laser Device

Photo-irradiation was performed using an 810-nm laser (Vari-Lase) operated in continuous (CW) and pulse (PW) modes. The laser beam was coupled into a 600-µm optical fiber to produce a 4-mm ($1/e^2$) circular spot on the nc-YSZ. The variable laser parameters were power (1-3 W) and pulse rate (0.3-5 Hz). Each combination of bacterial species, radiant exposure and frequency modulation was tested a total of nine times.

Temperature Measurements

The temperature of the surface of nc-YSZ was measured with a non-contact infrared thermal camera (A325sc, FLIR Systems Inc.) operating in video mode. The video was post-processed using ResearchIR software (FLIR ResearchIR4). According to specifications, the camera measures temperatures with a precision of 50 mK, has an accuracy of 2%, and a viewing angle of 5-60 degrees.

Statistical Analysis

The difference between sham-irradiation and laser-irradiated samples was statistically evaluated using analysis of variance for repeated measurements (ANOVA). When appropriate, post hoc analyses were performed with the Bonferroni's multiple comparisons test. All statistics were calculated using GraphPad Prism 5.01 (GraphPad Software, Inc., San Diego, CA). Changes were considered statistically significant when the *P* value was less than 0.05.

Results

Figure 5.2 shows normalized RLU of biofilm after 24h and the average surface temperature (ΔT) of nc-YSZ at the end of the 20-second laser treatment using CW laser with 1, 2, and 3 W of power and 20 seconds of exposure time to deliver a total of 20, 40, 60 J of energy, respectively. The results show that the decrease in the RLU value is statistically significant for all treated groups compared to control ($p < 0.05$) and that ΔT for the CW laser powers above 1W is above 10 ^{o}C, which is considered the critical threshold for thermal damage. When CW laser is used, the biofilm reduction seems to follow a linear relationship with ΔT and this in turn with bacteria reduction, suggesting an entirely photothermal mechanism of bacterial damage.

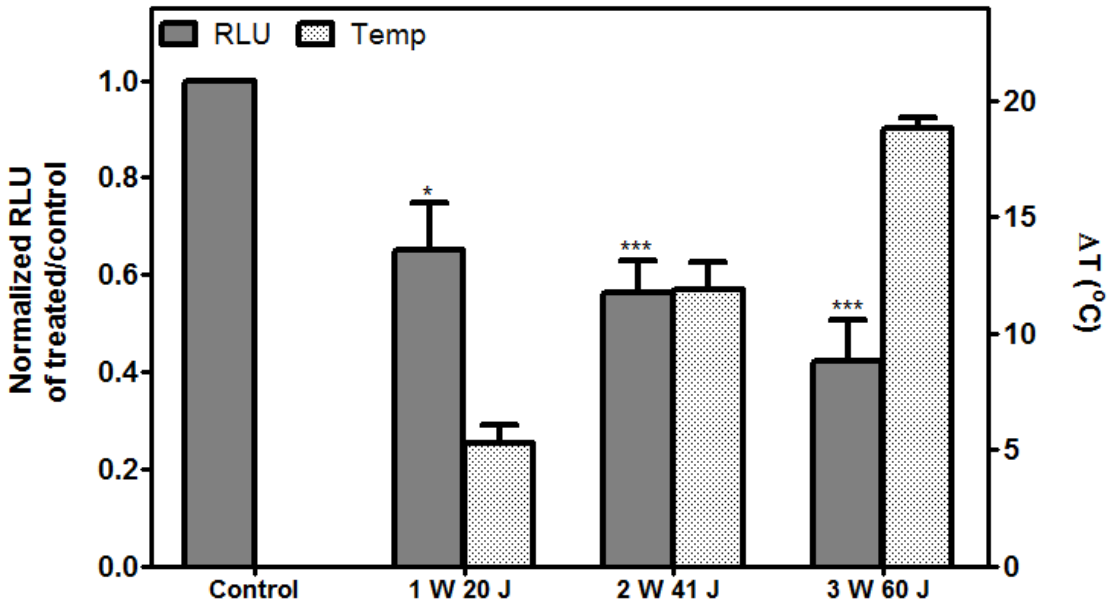

Figure 5.2. Normalized relative luminescence unit (RLU) of biofilm after 24h and the average surface temperature (ΔT) of nc-YSZ at the end of the 20-second laser treatment using CW laser with 1, 2, and 3 W of power and 20 seconds of exposure time to deliver a total of 20, 40, 60 J of energy, respectively. Each bar represents Mean ± SEM (n=9). 1-way ANOVA and Bonferroni's Multiple Comparison Test *p < 0.05, **P < 0.01, ***P < 0.001 relative to control.

Figure 5.3 shows normalized RLU of biofilm after 24h and the average surface temperature (ΔT) of nc-YSZ at the end of the 20-second CW or PW laser treatment as a result of laser treatment at 3 W, 60 J, 20 sec of exposure time. Treatment with all laser parameters except for 0.3 Hz leads to a significant reduction of E. coli viability compared to the control group ($p < 0.05$). The results indicate that the ΔT is above the 10 ^{o}C critical temperature threshold for CW laser and all the PW laser settings exceeding 5 J/cm^{2}and 1 Hz.

Comparing bar#3, bar#5, bar #6 and bar #7 (frequency of 5, 1, 0.5 and 0.3 Hz) indicates that laser treatment with higher frequency results in more reduction in E.coli biofilm. Comparing bar #4 and bar #5 (10 J/cm^2 400 ms vs. 5 J/cm^2 200 ms) indicates that doubling the energy density per pulse and pulse duration increases the temperature by about 3 ^{o}C while it has negligible effect on the reduction rate of E. coli biofilm.

The results indicate that CW laser has the higher reduction rate of E. coli biofilm compared to PW laser but also results in the highest increase in

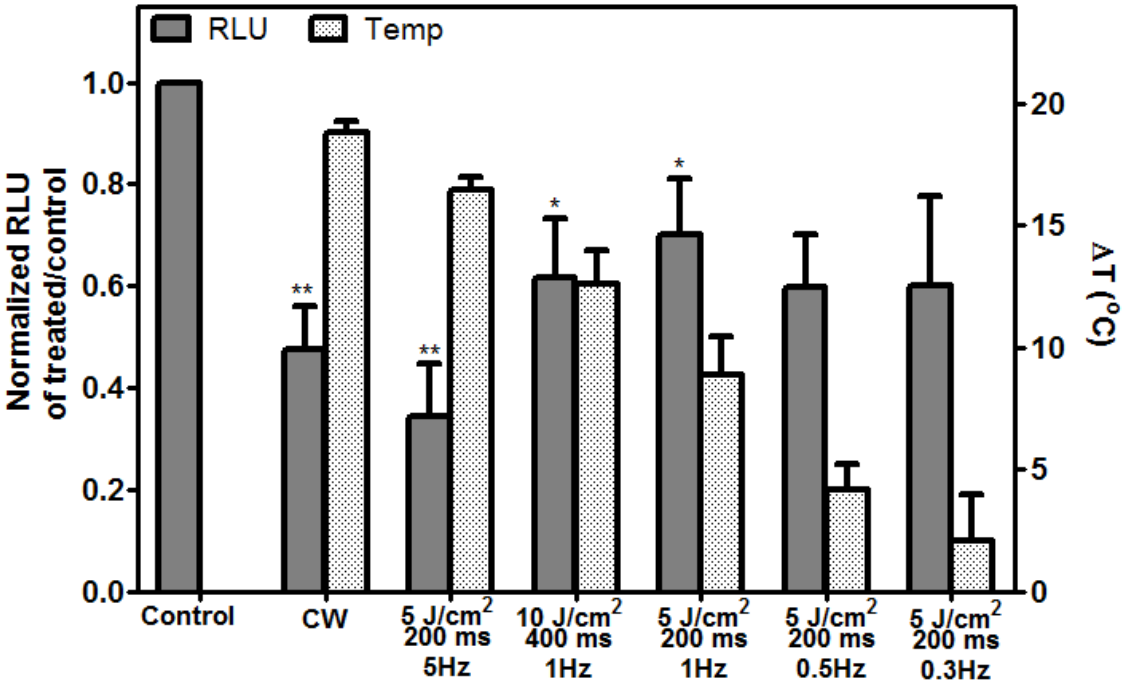

Figure 5.3. Normalized relative luminescence unit (RLU) of biofilm after 24h and the average surface temperature (ΔT) of nc-YSZ at the end of the 20-second laser treatment using 3W of power and 20 seconds of exposure time to deliver a total of 60J of energy with CW and PW modes. Each bar represents Mean ± SEM (n=9). 1-way ANOVA and Bonferroni's Multiple Comparison Test *p < 0.05, **P < 0.01, ***P < 0.001 relative to control.

temperature. In contrast to the linear relationship of temperature and biofilm reduction for CW laser, there is no linear relationship between the differences in temperature change and the distinct variability of the bactericidal effects of PW laser. Lack of correlation between ΔT and RLU suggests that the biofilm disruption mechanism using the PW mode is not entirely due to photothermal effects.

Discussion

WttB provides the transparency and toughness required for clinically-viable cranial implants for optical therapy and imaging of the brain [45]. Zirconia surfaces have lower bacteria adhesion compared to other implant materials [171], however, infection due to implants is the most significant risk factor associated with cranial implants independent of the implant material [111]. In almost all cases of cranial implant infection, it is recommended to remove and later replace the implant to avoid intradural propagation of the infection and the severe consequent risk [155]. Therefore, new treatment techniques are demanded as infections associated with cranial implants lead to chronic complications [172].

Various NIR diode lasers and Nd: YAG lasers are used successfully in endodontics for disinfection of almost all bacteria species. Diode lasers (λ=810nm) have been used to effectively reduce the viability of biofilm that adhered to zirconia dental implant surfaces. Stubinger et al. studied the effect of diode (λ=810), CO_2 (λ=10,600 nm) and Er:YAG laser (λ= 2,940 nm) on surface properties of yttria-stabilized tetragonal zirconia polycrystal (Y-TZP) implant surface using SEM, confocal 3D white light microscopy (CWLM) and energy-dispersive X-ray (EDX)

and demonstrated that currently, diode lasers seem to be the only laser systems offering surface preservation and safety in the treatment of peri-implantitis with zirconia [173]. Also, the transmission of nc-YSZ is approximately 35% at 810 nm wavelength [45], therefore only 35% of the laser energy directly comes in contact with the bacteria.

In a previous study, Nussbaum et al. [174] compared the effects of 810 nm (15 mW/cm^2; 1-50 J/cm^2) laser on E. coli using 3 W of power in CW or frequency modulated light at 26, 292, 1000, and 3800 Hz and demonstrated that the laser-mediated growth of E. coli was dependent on pulse frequency. Specifically, E. coli growth was increased when exposed to laser irradiation from CW up to a pulse frequency of 1000 Hz (2 J/cm^2) but was drastically inhibited at a pulse frequency of 3800 Hz and radiant exposure of 10 J/cm^2 . The authors suggested that higher pulse frequency might lead to greater accumulation of heat in the target cells when the pulse period plus the pulse interval are together shorter than thermal relaxation time. While this explanation seems plausible, the thermal relaxation times of either an isolated E. coli cell or a monolayer do not match. It has been established that single E. coli cells have a thermal diffusion time of 1 microseconds [175]. This means that in order to induce heat accumulation within an isolated E. coli cell and, thus, induce growth inhibition per the heat accumulation argument, frequencies larger than 1 MHz would have been necessary. On the other hand, a bacterial monolayer with thickness equivalent to an E. Coli cell diameter of 400 micrometers and a thermal diffusivity of water, yields a and estimated thermal diffusion time of

~ 70 ms (see footnote[1]). This corresponds to a characteristic frequency of ~ 14 Hz. If the transition between growth and inhibition is indeed frequency-mediated, the change from one to the other should be noted for pulse durations (plus time intervals between pulses) above and below ~ 70 ms (or corresponding pulse frequencies of 14 Hz). However, all chosen frequencies in this study were above 14 Hz.

In a follow up study, Nussbaum et al. [176] evaluated the relevance of irradiance and radiant exposure by comparing the effects of CW and PW modes of 810 nm laser irradiation with 3 W of power on the viability of E. coli in vitro with radiant exposure in the range of 1-50 J/cm^2. The results revealed that E. coli growth was increased when exposed to laser regardless of irradiance and the greatest rate of growth was observed for low radiant exposures (1-20 J/cm^2). The authors suggested that the increase in the bacterial growth was due to the increase of growth factor released from macrophage-like cells, stimulation of fibroblast and keratinocyte proliferation, and the increase of lymphocyte activity and angiogenesis. While this explanation is plausible, it is puzzling that only bacterial growth was observed especially for the very large radiant exposure used (up to 50

---

[1] $T_{sphere} = d^2/ (24.D)$ d=diameter D=diffusivity= 10^{-7} m^2/s

Volume of bacteria= 0.5 µL = 0.5 x 10^{-9} m^3

→ d= 0.0004 m

T_{sphere} = (4 x 10^-4)^2 / 24 x (10^-7)= 16/240=0.07 sec

J/cm^2), even when in their previous study they revealed inhibition with a fluence as low as 10 J/cm^2.

In our current study we selected frequencies even lower than what had been previously reported. Yet, all our results showed bacterial depletion It should be noted that in both previous studies [174, 176], the laser was applied directly on the E. coli that was grown on the agar plate. Here, our results show a sensible reduction of E.coli that is irradiated across the nc-YSZ implant (as quantified by the RLU). This can suggest that the increase in the surface temperature of nc-YSZ due to absorption of 810-nm light enhances the bactericidal effect of direct irradiation. In addition, nc-YSZ serves as a thermal barrier to the bacteria, preventing the thermal diffusion through convection and resulting in higher thermal energy in the biofilm layer. Even when the ΔT is about 2 ^{o}C (bar #7 in Figure 3), the bacterial growth reduced by about 40%, and while this reduction was not statistically significant, the clinical implication of reduction of E. coli biofilm by 40% would be considerable.

Although there has been several in vivo and in vitro reports demonstrating the bactericidal effect of medical lasers on various strains, the underlying mechanisms of photochemical or/and photothermal effects remain controversial. Lee et al demonstrated that heating of E. coli at 55 to 70 ^{o}C for 60 seconds decreases the viability significantly due to enthalpy change and irreversible damage to ribosomal subunits [177]. Using the temperature range of 50 to 70 ^{o}C and comparing temperature increase by CW high-power NIR laser (18 – 81 W/cm^2)

and water bath, Hibst et. al. showed that E. coli inactivation of E. coli suspension is mainly driven by a thermal process [178]. In this report, we were able to achieve a statistically significant decrease in the viability of E. coli on agar at a lower temperature using the lower-power CW and PW (as low as 41 ^{o}C for 20 sec with 3W, 5 J/cm^2 , 200 ms, 0.5 Hz, 7.8 W/cm^2), which may suggest a non-photothermal mechanism. The idea of non-photothermal mechanism of laser bacterial killing has also been explored previously [179, 180]. Lubart et al. reviewed the evidence that suggested reactive oxygen species (ROS) generation contributed to the phototoxic effect of NIR light [179]. Nandakumar et al. reported that the bactericidal effect of laser resulted in reduction in ATP production which could be due to damage of bacterial metabolic processes such as cellular respiration [180]. In the present study, the 810 nm laser light can have direct and indirect interaction with biofilm due to transmission of light through nc-YZ and the increase in the temperature of nc-YSZ, respectively. Therefore, while beyond the scope of this study, it is possible that more than one mechanism is contributing to the statistically significant reduction of biofilm viability.

Using lasers to remove the bacterial biofilm that might form under WttB in vivo will have lower local temperatures due to the presence of corticospinal fluid (CSF) that can act as a thermal barrier to the brain. The distance between the brain and the inner surface of the skull mapped by Fournier et al. [181] ranges from 0.4 to 6.7 mm. Therefore, depending on the actual location of the implant, this distance has to be considered in planning treatment. In addition, low-level laser therapy

(LLLT) using 810 nm lasers has been shown to significantly improve the neurobehavioral performance of mice after closed head traumatic brain injury (TBI) [182]. Therefore, with careful choice of 810 nm laser parameters, biofilm removal can be performed along with LLLT treatment of TBI.

In conclusion, the results of this study suggest that using nc-YSZ as a cranial implant may potentially lead to local, non-invasive, chronic treatment of the biofilm layer that might form on the inner surface of the cranial implant without inducing thermal damage to the underlying host tissue when appropriate laser parameters are used.

Acknowledgments

I would like to acknowledge the contribution of my co-authors to this study: Natalie De Howitt, Dr. Javier E. Garay and Dr. Guillermo Aguilar. This study was supported, in part, by the National Science Foundation (NSF) Award No. 1547014 to GA and JEG. The authors would like to acknowledge the UC-MEXUS Dissertation Research Grant awarded to YD to conduct this study. We would also like to thank the American Society for Lasers in Medicine and Surgery (ASLMS) for a travel grant awarded to YD to present research leading to this study at the 35th Annual ASLMS Conference, Kissimmee, FL April 2015. Additionally, we thank Dr. Yasuhiro Kodera for providing the nc-YSZ samples.

Chapter 6. Conclusions and Recommendations for Future work

In this dissertation, I demonstrated that transparency of nc-YSZ represents an excellent opportunity to use nc-YSZ as a cranial implant for laser and optogenetic therapy because light could be easily transmitted through it without undergoing excessive attenuation—the main obstacle for optical therapy and diagnostics of deep targets. Furthermore, transmission of light through homogeneous transparent cranial implants would not only open a “window” through which deeper brain targets could be imaged and or therapeutically treated, but would also allow for prolonged post-operatory interventions without the need for subsequent invasive therapies.

WttB can facilitate the non-invasive site-specific opening of the blood-brain barrier (BBB) and therefore enhance the delivery of anti-cancer drugs into the brain. BBB limits the passage of blood-borne agents into the CNS. Almost all large-molecule drugs and 98% of small molecules cannot cross the BBB [183]. Current techniques for disrupting the BBB include direct injection into the cerebrospinal fluid or tumor, implantation of catheters into the brain, and convection-enhanced delivery [184]. However, these techniques have not been clinically utilized due to several drawbacks including the need for repeated injection, high risk of infection, and limited drug diffusion. Optical techniques such as photodynamic therapy [185] and photochemical internalization (PCI) [186] can cause localized and temporary opening of the BBB with minimal damage to surrounding normal brain. Selective

disruption of the BBB optically via WttB, followed by administration of anti-cancer agents, could allow for non-invasive combinatorial photo-chemotherapy and the elimination of infiltrating gliomas.

WttB can further enhance optical access to the brain with: (a) waveguides written across its thickness facilitating usage of femtosecond laser irradiation with ultralow energies for targeting deeper brain tissue, and; (b) waveguides coupled to optical fibers to deliver laser light to the deepest targets when necessary.

The preliminary studies of biocompatibility presented in Chapter 4 have demonstrated that within the first two weeks of implantation, the nc-YSZ implants do not cause any significant change in microhemodynamics, microvascular permeability, or leukocyte-endothelial cell interaction. The biocompatibility of nc-YSZ can be further studied using a murine calvarial defect model to evaluate encapsulation and osseointegration responses. Morphological changes can be monitored using OCT at regular intervals over 30 days, including inflammatory response and granulation tissue formation [187]. Animals can be euthanized at 30 days post-surgery and the calvariae can be removed by dissecting the bone free from the underlying brain. The bone flaps surrounding the nc-YSZ implant and control can be fixed, sectioned, and stained with hematoxylin-eosin (H&E). Stained sections can then be imaged using a confocal microscope to quantify osteolytic lesions and residual bone.

It would also be beneficial to investigate the potential of nc-YSZ implant for facilitating non-invasive, OCT-based detection of cerebral edema using standard animal models already in use by Drs. Park and Binder. There are a number of quantitative measures to gauge any improvement. These include average backscattered intensity, and quality of focus, as determined by the sharpness of anatomical regions in OCT images. I anticipate that OCT through the native scalp overlaid on the nc-YSZ implant will cause scattering of visible and near-IR light, thus rendering the scalp opaque. To solve this, techniques presented in Chapter 3 on enhancing the perfusion of OCA can be applied to temporarily render the overlying scalp transparent on demand. If this proves insufficient, a micro-incision can be made using a CO_2 laser to deliver the OCT laser beam to the nc-YSZ implant. I expect the regions under the nc-YSZ implants and cleared (or removed) scalp to display vastly improved focus and light collection relative to native cranium and scalp.

In conclusion, my dissertation research has paved the way for expanding the collaboration opportunities between several UC Riverside, CICESE, UC San Diego, UNAM, INAOE, and Louisiana Tech research groups through the development of a new area of laser therapy and imaging of brains using this innovative transparent cranial implant. Replacing repeated craniotomies with one-time placement of nc-YSZ implants will prevent expensive and highly invasive craniotomies that are subject to potentially fatal complications. The resources and facilities at UCR have provided me with the opportunity to engage in collaborative

research to have a direct and timely implication for improving the quality of life of patients with brain pathologies by enhancing diagnostics and therapeutic tools.

References

1. C. B. T. R. o. t. U. States, "2014 CBTRUS Fact Sheet."

2. S. Larjavaara, R. Mantyla, T. Salminen, H. Haapasalo, J. Raitanen, J. Jaaskelainen, and A. Auvinen, "Incidence of gliomas by anatomic location," Neuro Oncol **9**, 319-325 (2007).

3. J. M. Legler, L. A. Ries, M. A. Smith, J. L. Warren, E. F. Heineman, R. S. Kaplan, and M. S. Linet, "Cancer surveillance series [corrected]: brain and other central nervous system cancers: recent trends in incidence and mortality," J Natl Cancer Inst **91**, 1382-1390 (1999).

4. M. A. Smith, E. Shahar, K. M. Doliszny, P. G. McGovern, D. K. Arnett, and R. V. Luepker, "Trends in medical care of hospitalized stroke patients between 1980 and 1990: the Minnesota Stroke Survey," J Stroke Cerebrovasc Dis **7**, 76-84 (1998).

5. M. Wrensch, Y. Minn, T. Chew, M. Bondy, and M. S. Berger, "Epidemiology of primary brain tumors: current concepts and review of the literature," Neuro Oncol **4**, 278-299 (2002).

6. U. Pichlmeier, A. Bink, G. Schackert, and W. Stummer, "Resection and survival in glioblastoma multiforme: an RTOG recursive partitioning analysis of ALA study patients," Neuro Oncol **10**, 1025-1034 (2008).

7. B. J. Quirk, G. Brandal, S. Donlon, J. C. Vera, T. S. Mang, A. B. Foy, S. M. Lew, A. W. Girotti, S. Jogal, P. S. LaViolette, J. M. Connelly, and H. T. Whelan, "Photodynamic therapy (PDT) for malignant brain tumors - where do we stand?," Photodiagnosis Photodyn Ther (2015).

8. D. Coluccia, J. Fandino, L. Schwyzer, R. O'Gorman, L. Remonda, J. Anon, E. Martin, and B. Werner, "First noninvasive thermal ablation of a brain tumor with MR-guided focused ultrasound," J Ther Ultrasound **2**, 17 (2014).

9. Y. Cheng, R. A. Morshed, B. Auffinger, A. L. Tobias, and M. S. Lesniak, "Multifunctional nanoparticles for brain tumor imaging and therapy," Advanced drug delivery reviews **66**, 42-57 (2014).

10. S. R. Finfer and J. Cohen, "Severe traumatic brain injury," Resuscitation **48**, 77-90 (2001).

11. W. Rutland-Brown, J. A. Langlois, K. E. Thomas, and Y. L. Xi, "Incidence of Traumatic Brain Injury in the United States, 2003," The Journal of Head Trauma Rehabilitation **21**, 544-548 (2006).

12. J. Nortje and D. K. Menon, "Traumatic brain injury: physiology, mechanisms, and outcome," Curr Opin Neurol **17**, 711-718 (2004).

13. M. R. Bullock and J. T. Povlishock, "Guidelines for the management of severe traumatic brain injury. Editor's Commentary," J Neurotrauma **24 Suppl 1**, 2 p preceding S1 (2007).

14. W. Xuan, T. Agrawal, L. Huang, G. K. Gupta, and M. R. Hamblin, "Low-level laser therapy for traumatic brain injury in mice increases brain derived neurotrophic factor (BDNF) and synaptogenesis," J Biophotonics **8**, 502-511 (2015).

15. Q. Zhang, C. Zhou, M. R. Hamblin, and M. X. Wu, "Low-level laser therapy effectively prevents secondary brain injury induced by immediate early responsive gene X-1 deficiency," J Cereb Blood Flow Metab **34**, 1391-1401 (2014).

16. E. S. Boyden, F. Zhang, E. Bamberg, G. Nagel, and K. Deisseroth, "Millisecond-timescale, genetically targeted optical control of neural activity," Nat Neurosci **8**, 1263-1268 (2005).

17. H. C. Tsai, F. Zhang, A. Adamantidis, G. D. Stuber, A. Bonci, L. de Lecea, and K. Deisseroth, "Phasic firing in dopaminergic neurons is sufficient for behavioral conditioning," Science **324**, 1080-1084 (2009).

18. C. P. Goold and R. A. Nicoll, "Single-cell optogenetic excitation drives homeostatic synaptic depression," Neuron **68**, 512-528 (2010).

19. A. Peled, "Optogenetic neuronal control in schizophrenia," Med Hypotheses **76**, 914-921 (2011).

20. M. Kokaia and A. T. Sorensen, "The treatment of neurological diseases under a new light: the importance of optogenetics," Drugs Today (Barc) **47**, 53-62 (2011).

21. A. Rolls, D. Colas, A. Adamantidis, M. Carter, T. Lanre-Amos, H. C. Heller, and L. de Lecea, "Optogenetic disruption of sleep continuity impairs memory consolidation," Proc Natl Acad Sci U S A **108**, 13305-13310 (2011).

22. G. D. Stuber, "Dissecting the neural circuitry of addiction and psychiatric disease with optogenetics," Neuropsychopharmacology **35**, 341-342 (2010).

23. J. Tonnesen, C. L. Parish, A. T. Sorensen, A. Andersson, C. Lundberg, K. Deisseroth, E. Arenas, O. Lindvall, and M. Kokaia, "Functional integration of grafted neural stem cell-derived dopaminergic neurons monitored by optogenetics in an in vitro Parkinson model," PLoS One **6**, e17560 (2011).

24. V. Gradinaru, F. Zhang, C. Ramakrishnan, J. Mattis, R. Prakash, I. Diester, I. Goshen, K. R. Thompson, and K. Deisseroth, "Molecular and cellular approaches for diversifying and extending optogenetics," Cell **141**, 154-165 (2010).

25. K. Deisseroth, "Optogenetics," Nat Methods **8**, 26-29 (2011).

26. O. Yizhar, L. E. Fenno, T. J. Davidson, M. Mogri, and K. Deisseroth, "Optogenetics in neural systems," Neuron **71**, 9-34 (2011).

27. C. G. Hadjipanayis, H. Jiang, D. W. Roberts, and L. Yang, "Current and future clinical applications for optical imaging of cancer: from intraoperative surgical guidance to cancer screening," Semin Oncol **38**, 109-118 (2011).

28. S. F. Hulbert, "THE USE OF ALUMINA AND ZIRCONIA IN SURGICAL IMPLANTS," in *An Introduction To Bioceramics*, pp. 25-40.

29. A. Rovira, J. Cordoba, N. Raguer, and J. Alonso, "Magnetic resonance imaging measurement of brain edema in patients with liver disease: resolution after transplantation," Current Opinion in Neurology **15**, 731-737 (2002).

30. J. Vaquero, R. J. Fontana, A. M. Larson, N. M. Bass, T. J. Davern, A. O. Shakil, S. Han, M. E. Harrison, T. R. Stravitz, S. Munoz, R. Brown, W. M. Lee, and A. T. Blei, "Complications and use of intracranial pressure monitoring in patients with acute liver failure and severe encephalopathy," Liver transplantation : official publication of the American Association for the Study of Liver Diseases and the International Liver Transplantation Society **11**, 1581-1589 (2005).

31. P. R. Salvalaggio, T. B. Baker, A. J. Koffron, J. P. Fryer, L. Clark, R. A. Superina, A. T. Blei, A. Nemcek, and M. M. Abecassis, "Liver graft volume estimation in 100 living donors: measure twice, cut once," Transplantation **80**, 1181-1185 (2005).

32. S. M. Kurtz and J. N. Devine, "PEEK biomaterials in trauma, orthopedic, and spinal implants," Biomaterials **28**, 4845-4869 (2007).

33. P. Christel, A. Meunier, M. Heller, J. P. Torre, and C. N. Peille, "Mechanical properties and short-term in-vivo evaluation of yttrium-oxide-partially-stabilized zirconia," Journal of biomedical materials research **23**, 45-61 (1989).

34. K. Nakamura, T. Kanno, P. Milleding, and U. Ortengren, "Zirconia as a dental implant abutment material: a systematic review," The International journal of prosthodontics **23**, 299-309 (2010).

35. P. Christel, A. Meunier, J. M. Dorlot, J. M. Crolet, J. Witvoet, L. Sedel, and P. Boutin, "Biomechanical compatibility and design of ceramic implants for orthopedic surgery," Annals of the New York Academy of Sciences **523**, 234-256 (1988).

36. E. H. Jordan, C. Jiang, J. Roth, and M. Gell, "Low Thermal Conductivity Yttria-Stabilized Zirconia Thermal Barrier Coatings Using the Solution Precursor Plasma Spray Process," Journal of Thermal Spray Technology **23**, 849-859 (2014).

37. J. E. Alaniz, F. G. Perez-Gutierrez, G. Aguilar, and J. E. Garay, "Optical properties of transparent nanocrystalline yttria stabilized zirconia," Opt Mater **32**, 62-68 (2009).

38. J. E. Garay, S. R. Casolco, and J. Xu, "Transparent/translucent polycrystalline nanostructured yttria stabilized zirconia with varying colors," Scr. Mater. **58**, 516-519 (2008).

39. J. G. Fujimoto, M. E. Brezinski, G. J. Tearney, S. A. Boppart, B. Bouma, M. R. Hee, J. F. Southern, and E. A. Swanson, "Optical biopsy and imaging using optical coherence tomography," Nature medicine **1**, 970-972 (1995).

40. J. G. Fujimoto, C. Pitris, S. A. Boppart, and M. E. Brezinski, "Optical coherence tomography: an emerging technology for biomedical imaging and optical biopsy," Neoplasia **2**, 9-25 (2000).

41. A. D. Aguirre, Y. Chen, J. G. Fujimoto, L. Ruvinskaya, A. Devor, and D. A. Boas, "Depth-resolved imaging of functional activation in the rat cerebral cortex using optical coherence tomography," Opt Lett **31**, 3459-3461 (2006).

42. Y. Wang, C. M. Oh, M. C. Oliveira, M. S. Islam, A. Ortega, and B. H. Park, "GPU accelerated real-time multi-functional spectral-domain optical coherence tomography system at 1300nm," Opt Express **20**, 14797-14813 (2012).

43. E. M. Szu JI, Reynolds CL, Hsu MS, Park BH, Binder DK, "Thinned-skull cortical window technique for in vivo optical coherence tomography imaging," Journal of Visualized Experiments **in press**(2012).

44. Y. Damestani, B. Melakeberhan, M. P. Rao, and G. Aguilar, "Optical clearing agent perfusion enhancement via combination of microneedle poration, heating and pneumatic pressure," Lasers Surg Med **46**, 488-498 (2014).

45. Y. Damestani, C. L. Reynolds, J. Szu, M. S. Hsu, Y. Kodera, D. K. Binder, B. H. Park, J. E. Garay, M. P. Rao, and G. Aguilar, "Transparent nanocrystalline yttria-stabilized-zirconia calvarium prosthesis," Nanomedicine : nanotechnology, biology, and medicine **9**, 1135-1138 (2013).

46. A window to the brain? It's here, says UC Riverside team", Los Angeles Times, 4 September 2013 http://articles.latimes.com/2013/sep/04/science/la-sci-sn-window-brain-20130903

47. A. F. Zuluaga, R. Drezek, T. Collier, R. Lotan, M. Follen, and R. Richards-Kortum, "Contrast agents for confocal microscopy: how simple chemicals affect confocal images of normal and cancer cells in suspension," Journal of Biomedical Optics **7**, 398-403 (2002).

48. I. V. Meglinski, A. N. Bashkatov, E. A. Genina, D. Y. Churmakov, and V. V. Tuchin, "The enhancement of confocal images of tissues at bulk optical immersion," Laser Phys **13**, 65-69 (2003).

49. V. V. Tuchin, "Optical clearing of tissues and blood using the immersion method," J Phys D Appl Phys **38**, 2497-2518 (2005).

50. J. Jiang and R. K. Wang, "Comparing the synergistic effects of oleic acid and dimethyl sulfoxide as vehicles for optical clearing of skin tissue in vitro," Phys Med Biol **49**, 5283-5294 (2004).

51. A. T. Yeh, B. Choi, J. S. Nelson, and B. J. Tromberg, "Reversible dissociation of collagen in tissues," J Invest Dermatol **121**, 1332-1335 (2003).

52. X. Xu and Q. Zhu, "Evaluation of skin optical clearing enhancement with Azone as a penetration enhancer," Optics Communications **279**, 223-228 (2007).

53. G. Vargas, E. K. Chan, J. K. Barton, H. G. Rylander, 3rd, and A. J. Welch, "Use of an agent to reduce scattering in skin," Lasers Surg Med **24**, 133-141 (1999).

54. Y. He and R. K. Wang, "Dynamic optical clearing effect of tissue impregnated with hyperosmotic agents and studied with optical coherence tomography," J Biomed Opt **9**, 200-206 (2004).

55. E. I. Galanzha, V. V. Tuchin, A. V. Solovieva, T. V. Stepanova, Q. Luo, and H. Cheng, "Skin backreflectance and microvascular system functioning at the action of osmotic agents," J Phys D Appl Phys **36**, 1739-1746 (2003).

56. X. Wen, Z. Mao, Z. Han, V. V. Tuchin, and D. Zhu*, "In vivo skin optical clearing by glycerol solutions: mechanism," Journal of Biophotonics **3**, 44-52 (2010).

57. M. A. Naeser and M. R. Hamblin, "Potential for Transcranial Laser or LED Therapy to Treat Stroke, Traumatic Brain Injury, and Neurodegenerative Disease," Photomedicine and Laser Surgery **29**, 443-446 (2011).

58. M. S. Mathews, D. Chighvinadze, H. M. Gach, F. A. Uzal, S. J. Madsen, and H. Hirschberg, "Cerebral edema following photodynamic therapy using endogenous and exogenous photosensitizers in normal brain," Lasers Surg Med **43**, 892-900 (2011).

59. P. Juzenas, W. Chen, Y. P. Sun, M. A. N. Coelho, R. Generalov, N. Generalova, and I. L. Christensen, "Quantum dots and nanoparticles for photodynamic and radiation therapies of cancer," Adv Drug Deliver Rev **60**, 1600-1614 (2008).

60. J. I. Szu, M. M. Eberle, C. L. Reynolds, M. S. Hsu, Y. Wang, C. M. Oh, M. S. Islam, B. H. Park, and D. K. Binder, "Thinned-skull cortical window technique for in vivo optical coherence tomography imaging," Journal of visualized experiments : JoVE, e50053 (2012).

61. E. A. Kelly and A. K. Majewska, "Chronic imaging of mouse visual cortex using a thinned-skull preparation," Journal of visualized experiments : JoVE (2010).

62. R. Mostany and C. Portera-Cailliau, "A craniotomy surgery procedure for chronic brain imaging," Journal of visualized experiments : JoVE (2008).

63. P. J. Drew, A. Y. Shih, J. D. Driscoll, P. M. Knutsen, P. Blinder, D. Davalos, K. Akassoglou, P. S. Tsai, and D. Kleinfeld, "Chronic optical access through a polished and reinforced thinned skull," Nature methods **7**, 981-984 (2010).

64. R. L. Coble, "Diffusion Models for Hot Pressing with Surface Energy and Pressure Effects as Driving Forces," J. Appl. Phys. **85**(1970).

65. J. E. Garay, "Current-Activated, Pressure-Assisted Densification of Materials," Annu Rev Mater Res **40**, 445-468 (2010).

66. A. Y. Shih, C. Mateo, P. J. Drew, P. S. Tsai, and D. Kleinfeld, "A polished and reinforced thinned-skull window for long-term imaging of the mouse brain," Journal of visualized experiments : JoVE (2012).

67. A. Villringer, A. Them, U. Lindauer, K. Einhaupl, and U. Dirnagl, "Capillary perfusion of the rat brain cortex. An in vivo confocal microscopy study," Circ Res **75**, 55-62 (1994).

68. S. W. Jeon, M. A. Shure, K. B. Baker, D. Huang, A. M. Rollins, A. Chahlavi, and A. R. Rezai, "A feasibility study of optical coherence tomography for guiding deep brain probes," Journal of neuroscience methods **154**, 96-101 (2006).

69. A. N. Yaroslavsky, P. C. Schulze, I. V. Yaroslavsky, R. Schober, F. Ulrich, and H. J. Schwarzmaier, "Optical properties of selected native and coagulated human brain tissues in vitro in the visible and near infrared spectral range," Phys Med Biol **47**, 2059-2073 (2002).

70. R. Cicchi, D. Sampson, D. Massi, and F. Pavone, "Contrast and depth enhancement in two-photon microscopy of human skin ex vivo by use of optical clearing agents," Opt Express **13**, 2337-2344 (2005).

71. V. V. Tuchin, I. L. Maksimova, D. A. Zimnyakov, I. L. Kon, A. H. Mavlyutov, and A. A. Mishin, "Light propagation in tissues with controlled optical properties," Journal of Biomedical Optics **2**, 401-417 (1997).

72. G. Vargas, K. F. Chan, S. L. Thomsen, and A. J. Welch, "Use of osmotically active agents to alter optical properties of tissue: effects on the detected fluorescence signal measured through skin," Lasers Surg Med **29**, 213-220 (2001).

73. J. Cordoba and A. T. Blei, "Cerebral edema and intracranial pressure monitoring," Liver Transplantation and Surgery **1**, 187-194 (1995).

74. E. A. Popovic, A. H. Kaye, and J. S. Hill, "Photodynamic therapy of brain tumors," Journal of clinical laser medicine & surgery **14**, 251-261 (1996).

75. J. Wang, I. Ozden, M. Diagne, F. Wagner, D. Borton, B. Brush, N. Agha, R. Burwell, D. Sheinberg, I. Diester, K. Deisseroth, and A. Nurmikko, "Approaches to optical neuromodulation from rodents to non-human primates by integrated optoelectronic devices.," in *Conf Proc IEEE Eng Med Biol Soc.*, 2011), 7525-7528.

76. B. Chance, C. Robertson, S. Gopinath, H. Liu, Y. Zhang, and A. Mayevsky, "Optical response to osmotic stress and cortical depolarization in animal brain.," Biophys J **70**, Wp154-Wp154 (1996).

77. J. S. Maier, S. A. Walker, S. Fantini, M. A. Franceschini, and E. Gratton, "Possible correlation between blood glucose concentration and the reduced scattering coefficient of tissues in the near infrared," Opt Lett **19**, 2062-2064 (1994).

78. I. V. Yaroslavsky, A. N. Yaroslavsky, V. V. Tuchin, and H. J. Schwarzmaier, "Effect of the scattering delay on time-dependent photon migration in turbid media," Appl Opt **36**, 6529-6538 (1997).

79. D. A. Zimnyakov, V. V. Tuchin, and A. A. Mishin, "Spatial speckle correlometry in applications to tissue structure monitoring," Appl Opt **36**, 5594-5607 (1997).

80. R. K. Wang and M. Wilson, "Vertex/propagator model for least-scattered photons traversing a turbid medium," J Opt Soc Am A Opt Image Sci Vis **18**, 224-231 (2001).

81. R. K. Wang, "Signal degradation by multiple scattering in optical coherence tomography of dense tissue: a Monte Carlo study towards optical clearing of biotissues," Phys Med Biol **47**, 2281-2299 (2002).

82. X. Xu, R. K. Wang, and A. El Haj, "Investigation of changes in optical attenuation of bone and neuronal cells in organ culture or three-dimensional constructs in vitro with optical coherence tomography: relevance to cytochrome oxidase monitoring," Eur Biophys J **32**, 355-362 (2003).

83. M. H. Khan, S. Chess, B. Choi, K. M. Kelly, and J. S. Nelson, "Can topically applied optical clearing agents increase the epidermal damage

threshold and enhance therapeutic efficacy?," Lasers Surg Med **35**, 93-95 (2004).

84. R. J. McNichols, M. A. Fox, A. Gowda, S. Tuya, B. Bell, and M. Motamedi, "Temporary dermal scatter reduction: quantitative assessment and implications for improved laser tattoo removal," Lasers Surg Med **36**, 289-296 (2005).

85. T. Han and D. B. Das, "Permeability enhancement for transdermal delivery of large molecule using low-frequency sonophoresis combined with microneedles," Journal of pharmaceutical sciences **102**, 3614-3622 (2013).

86. O. Stumpp, B. Chen, and A. J. Welch, "Using sandpaper for noninvasive transepidermal optical skin clearing agent delivery," J Biomed Opt **11**, 041118 (2006).

87. Z. Deng, C. Liu, W. Tao, and D. Zhu, "Improvement of skin optical clearing efficacy by topical treatment of glycerol at different temperatures," Journal of Physics: Conference Series 277 (2011).

88. A. R. Moritz and F. C. Henriques, "Studies of Thermal Injury: II. The Relative Importance of Time and Surface Temperature in the Causation of Cutaneous Burns," The American journal of pathology **23**, 695-720 (1947).

89. G. Aguilar, B. Choi, M. Broekgaarden, O. Yang, B. Yang, P. Ghasri, J. K. Chen, R. Bezemer, J. S. Nelson, A. M. van Drooge, A. Wolkerstorfer, K. M. Kelly, and M. Heger, "An overview of three promising mechanical, optical, and biochemical engineering approaches to improve selective photothermolysis of refractory port wine stains," Annals of biomedical engineering **40**, 486-506 (2012).

90. C. G. Rylander, T. E. Milner, S. A. Baranov, and J. S. Nelson, "Mechanical tissue optical clearing devices: enhancement of light penetration in ex vivo porcine skin and adipose tissue," Lasers Surg Med **40**, 688-694 (2008).

91. F. Netzlaff, U. F. Schaefer, C. M. Lehr, P. Meiers, J. Stahl, M. Kietzmann, and F. Niedorf, "Comparison of bovine udder skin with human and porcine skin in percutaneous permeation experiments," Alternatives to laboratory animals : ATLA **34**, 499-513 (2006).

92. R. L. Bronaugh, R. F. Stewart, E. R. Congdon, and A. L. Giles, Jr., "Methods for in vitro percutaneous absorption studies. I. Comparison with in vivo results," Toxicology and applied pharmacology **62**, 474-480 (1982).

93. X. Guo, Z. Guo, H. Wei, H. Yang, Y. He, S. Xie, G. Wu, X. Deng, Q. Zhao, and L. Li, "In vivo comparison of the optical clearing efficacy of optical clearing agents in human skin by quantifying permeability using optical coherence tomography," Photochemistry and photobiology **87**, 734-740 (2011).

94. Z. W. Zhi, Z. Z. Han, Q. M. Luo, and D. Zhu, "Improve Optical Clearing of Skin in Vitro with Propylene Glycol as a Penetration Enhancer," J Innov Opt Heal Sci **2**, 269-278 (2009).

95. T. F. Sun and A. S. Teja, "Density, viscosity and thermal conductivity of aqueous solutions of propylene glycol, dipropylene glycol, and tripropylene glycol between 290 K and 460 K," J Chem Eng Data **49**, 1311-1317 (2004).

96. X. Wang, Y. Pang, G. Ku, X. Xie, G. Stoica, and L. V. Wang, "Noninvasive laser-induced photoacoustic tomography for structural and functional in vivo imaging of the brain," Nature biotechnology **21**, 803-806 (2003).

97. M. H. Schmidt, D. M. Bajic, K. W. Reichert, 2nd, T. S. Martin, G. A. Meyer, and H. T. Whelan, "Light-emitting diodes as a light source for intraoperative photodynamic therapy," Neurosurgery **38**, 552-556; discussion 556-557 (1996).

98. M. Wolf, M. Ferrari, and V. Quaresima, "Progress of near-infrared spectroscopy and topography for brain and muscle clinical applications," J Biomed Opt **12**, 062104 (2007).

99. H. Hirschberg and Y. J. Kwon, "Photochemical Internalization (PCI)-Enhanced Nonviral Gene-Directed Enzyme Prodrug Cancer Therapy," Mol Ther **21**, S85-S86 (2013).

100. D. R. Wyman, S. W. Schatz, and J. A. Maguire, "Comparison of 810 nm and 1064 nm wavelengths for interstitial laser photocoagulation in rabbit brain," Lasers Surg Med **21**, 50-58 (1997).

101. S. A. Prahl, M. J. C. Vangemert, and A. J. Welch, "Determining the Optical-Properties of Turbid Media by Using the Adding-Doubling Method," Appl Optics **32**, 559-568 (1993).

102. A. J. Welch and M. J. C. van Gemert, *Optical-Thermal Response of Laser-Irradiated Tissue* (Springer, 2011).

103. J. P. Padilla-Martinez, J. C. Ramirez-San-Juan, N. Korneev, D. Banks, G. Aguilar, and R. Ramos-Garcia, "Breaking the Rayleigh-Plateau Instability

Limit Using Thermocavitation within a Droplet," Atomization Spray **23**, 487-503 (2013).

104. L. F. Devia-Cruz, F. G. Perez-Gutierrez, D. Garcia-Casillas, G. Aguilar, S. Camacho-Lopez, and D. Banks, "High Resolution Optical Experimental Technique for Computing Pulsed Laser-Induced Cavitation Bubble Dynamics in a Single Shot," Atomization Spray **23**, 475-485 (2013).

105. J. Yoon, T. Son, E. H. Choi, B. Choi, J. S. Nelson, and B. Jung, "Enhancement of optical skin clearing efficacy using a microneedle roller," J Biomed Opt **13**, 021103 (2008).

106. A. Izquierdo-Roman, W. C. Vogt, L. Hyacinth, and C. G. Rylander, "Mechanical tissue optical clearing technique increases imaging resolution and contrast through ex vivo porcine skin," Lasers Surg Med **43**, 814-823 (2011).

107. H.-J. Chun and H.-J. Yi, "Efficacy and safety of early cranioplasty, at least within 1 month," Journal of Craniofacial Surgery **22**, 203-207 (2011).

108. P. A. Winkler, W. Stummer, R. Linke, K. G. Krishnan, and K. Tatsch, "Influence of cranioplasty on postural blood flow regulation, cerebrovascular reserve capacity, and cerebral glucose metabolism," Journal of neurosurgery **93**, 53-61 (2000).

109. L. Chiarini, S. Figurelli, G. Pollastri, E. Torcia, F. Ferrari, M. Albanese, and P. Francesco Nocini, "Cranioplasty using acrylic material: a new technical procedure," Journal of Cranio-Maxillofacial Surgery **32**, 5-9 (2004).

110. B. Rodríguez, A. Romero, O. Soto, and O. de Varorna, "Biomaterials for orthopedics," Applications of Engineering Mechanics in Medicine, 1-26 (2004).

111. Y. R. Cho and A. K. Gosain, "Biomaterials in craniofacial reconstruction," Clinics in plastic surgery **31**, 377-385, v (2004).

112. E. T. Camarini, J. K. Tomeh, R. R. Dias, and E. J. da Silva, "Reconstruction of frontal bone using specific implant polyether-ether-ketone," J Craniofac Surg **22**, 2205-2207 (2011).

113. E. Heissler, F. S. Fischer, S. Bolouri, T. Lehmann, W. Mathar, A. Gebhardt, W. Lanksch, and J. Bier, "Custom-made cast titanium implants produced with CAD/CAM for the reconstruction of cranium defects," Int J Oral Maxillofac Surg **27**, 334-338 (1998).

114. A. Katzer, H. Marquardt, J. Westendorf, J. V. Wening, and G. von Foerster, "Polyetheretherketone--cytotoxicity and mutagenicity in vitro," Biomaterials **23**, 1749-1759 (2002).

115. L. Eschbach, "Nonresorbable polymers in bone surgery," Injury **31 Suppl 4**, 22-27 (2000).

116. K. L. Wong, C. T. Wong, W. C. Liu, H. B. Pan, M. K. Fong, W. M. Lam, W. L. Cheung, W. M. Tang, K. Y. Chiu, K. D. Luk, and W. W. Lu, "Mechanical properties and in vitro response of strontium-containing hydroxyapatite/polyetheretherketone composites," Biomaterials **30**, 3810-3817 (2009).

117. I. Y. Chang, "Pekk as a New Thermoplastic Matrix for High-Performance Composites," Sampe Quart **19**, 29-34 (1988).

118. I. Y. Chang and J. K. Lees, "Recent Development in Thermoplastic Composites: A Review of Matrix Systems and Processing Methods," Journal of Thermoplastic Composite Materials **1**, 277-296 (1988).

119. Y. Kodera, C. L. Hardin, and J. E. Garay, "Transmitting, emitting and controlling light: Processing of transparent ceramics using current-activated pressure-assisted densification," Scripta Mater **69**, 149-154 (2013).

120. H. Naderi, M. M. Matin, and A. R. Bahrami, "Review paper: critical issues in tissue engineering: biomaterials, cell sources, angiogenesis, and drug delivery systems," Journal of biomaterials applications **26**, 383-417 (2011).

121. J. M. Anderson, A. Rodriguez, and D. T. Chang, "Foreign body reaction to biomaterials," Semin Immunol **20**, 86-100 (2008).

122. P. Thevenot, W. Hu, and L. Tang, "Surface chemistry influences implant biocompatibility," Curr Top Med Chem **8**, 270-280 (2008).

123. R. T. Tran, P. Thevenot, Y. Zhang, D. Gyawali, L. Tang, and J. Yang, "Scaffold Sheet Design Strategy for Soft Tissue Engineering," Nat Mater **3**, 1375-1389 (2010).

124. F. Velard, D. Laurent-Maquin, J. Braux, C. Guillaume, S. Bouthors, E. Jallot, J. M. Nedelec, A. Belaaouaj, and P. Laquerriere, "The effect of zinc on hydroxyapatite-mediated activation of human polymorphonuclear neutrophils and bone implant-associated acute inflammation," Biomaterials **31**, 2001-2009 (2010).

125. P. M. Kou and J. E. Babensee, "Macrophage and dendritic cell phenotypic diversity in the context of biomaterials," J Biomed Mater Res A **96**, 239-260 (2011).

126. Z. Xia and J. T. Triffitt, "A review on macrophage responses to biomaterials," Biomed Mater **1**, R1-9 (2006).

127. M. Laschke, B. Vollmar, and M. Menger, "The dorsal skinfold chamber: window into the dynamic interaction of biomaterials with their surrounding host tissue," Eur Cell Mater **22**, 147-164 (2011).

128. M. D. Menger, M. W. Laschke, and B. Vollmar, "Viewing the microcirculation through the window: some twenty years experience with the hamster dorsal skinfold chamber," European Surgical Research **34**, 83-91 (2002).

129. P. Cabrales and A. G. Tsai, "Plasma viscosity regulates systemic and microvascular perfusion during acute extreme anemic conditions," American Journal of Physiology-Heart and Circulatory Physiology **291**, H2445-H2452 (2006).

130. B. Roetman, A. Ring, S. Langer, T. A. Schildhauer, G. Muhr, and M. Koller, "Microvascular response to calcium phosphate bone substitutes: an intravital microscopy analysis," Langenbecks Arch Surg **395**, 1147-1155 (2010).

131. C. N. Kraft, W. Weber, B. Burian, D. Zander, T. Wallny, O. Schmitt, and O. Diedrich, "[Striated muscle microvascular response to implants with sol-gel calcium phosphate coating. A comparative in vivo study]," Z Orthop Ihre Grenzgeb **140**, 672-680 (2002).

132. C. N. Kraft, M. Hansis, S. Arens, M. D. Menger, and B. Vollmar, "Striated muscle microvascular response to silver implants: A comparative in vivo study with titanium and stainless steel," Journal of biomedical materials research **49**, 192-199 (2000).

133. C. N. Kraft, B. Burian, O. Diedrich, J. Gessmann, M. A. Wimmer, and P. H. Pennekamp, "Microvascular response of striated muscle to common arthroplasty-alloys: A comparative in vivo study with CoCrMo, Ti-6Al-4V, and Ti-6Al-7Nb," J Biomed Mater Res A **75**, 31-40 (2005).

134. P. H. Pennekamp, J. Gessmann, O. Diedrich, B. Burian, M. A. Wimmer, V. M. Frauchiger, and C. N. Kraft, "Short-term microvascular response of striated muscle to cp-Ti, Ti-6Al-4V, and Ti-6Al-7Nb," Journal of

orthopaedic research : official publication of the Orthopaedic Research Society **24**, 531-540 (2006).

135. Institute of Laboratory Animal Resources (U.S.). Committee on Care and Use of Laboratory Animals., *Guide for the care and use of laboratory animals,* 8th ed. (National Academies Press, Washington, D.C., 2011), pp. xxv, 220 p.

136. B. Endrich, K. Asaishi, A. Gotz, and K. Messmer, "Technical report--a new chamber technique for microvascular studies in unanesthetized hamsters," Res Exp Med (Berl) **177**, 125-134 (1980).

137. A. Colantuoni, S. Bertuglia, and M. Intaglietta, "Quantitation of rhythmic diameter changes in arterial microcirculation," Am J Physiol **246**, H508-517 (1984).

138. P. Cabrales, A. G. Tsai, J. A. Frangos, and M. Intaglietta, "Role of endothelial nitric oxide in microvascular oxygen delivery and consumption," Free Radic Biol Med **39**, 1229-1237 (2005).

139. M. Intaglietta and W. R. Tompkins, "Microvascular measurements by video image shearing and splitting," Microvasc Res **5**, 309-312 (1973).

140. D. Ortiz and P. Cabrales, "Microhemodynamic parameters quantification from intravital microscopy videos," Physiol Meas **35**, 351 (2014).

141. H. H. Lipowsky and B. W. Zweifach, "Application of the "two-slit" photometric technique to the measurement of microvascular volumetric flow rates," Microvasc Res **15**, 93-101 (1978).

142. E. W. Childs, K. F. Udobi, J. G. Wood, F. A. Hunter, D. M. Smalley, and L. Y. Cheung, "*In vivo* visualization of reactive oxidants and leukocyte-endothelial adherence following hemorrhagic shock," Shock **18**, 423-427 (2002).

143. A. K. Behrendt, M. Beythien, J. Huber, T. Zufrass, A. Butschkau, T. Mittlmeier, and B. Vollmar, "New TiAg composite coating for bone prosthesis engineering shows promising microvascular compatibility in the murine dorsal skinfold chamber model," J Mater Sci Mater Med **26**, 5373 (2015).

144. M. W. Laschke, B. Vollmar, and M. D. Menger, "The dorsal skinfold chamber: window into the dynamic interaction of biomaterials with their surrounding host tissue," Eur Cell Mater **22**, 147-164; discussion 164-147 (2011).

145. M. D. Menger, M. W. Laschke, and B. Vollmar, "Viewing the microcirculation through the window: some twenty years experience with the hamster dorsal skinfold chamber," Eur Surg Res **34**, 83-91 (2002).

146. H. Liu and T. J. Webster, "Nanomedicine for implants: a review of studies and necessary experimental tools," Biomaterials **28**, 354-369 (2007).

147. S. Briggs, R. Ellis-Pegler, N. Raymond, M. Thomas, and L. Wilkinson, "Gram-negative bacillary meningitis after cranial surgery or trauma in adults," Scandinavian journal of infectious diseases **36**, 165-173 (2004).

148. H. J. Busscher, R. J. Ploeg, and H. C. van der Mei, "SnapShot: Biofilms and biomaterials; mechanisms of medical device related infections," Biomaterials **30**, 4247-4248 (2009).

149. C. R. Gordon, M. Fisher, J. Liauw, I. Lina, V. Puvanesarajah, S. Susarla, A. Coon, M. Lim, A. Quinones-Hinojosa, J. Weingart, G. Colby, A. Olivi, and J. Huang, "Multidisciplinary approach for improved outcomes in secondary cranial reconstruction: introducing the pericranial-onlay cranioplasty technique," Neurosurgery **10 Suppl 2**, 179-189; discussion 189-190 (2014).

150. A. Moreira-Gonzalez, I. T. Jackson, T. Miyawaki, K. Barakat, and V. DiNick, "Clinical outcome in cranioplasty: critical review in long-term follow-up," The Journal of craniofacial surgery **14**, 144-153 (2003).

151. F. L. Stephens, C. M. Mossop, R. S. Bell, T. Tigno, Jr., M. K. Rosner, A. Kumar, L. E. Moores, and R. A. Armonda, "Cranioplasty complications following wartime decompressive craniectomy," Neurosurgical focus **28**, E3 (2010).

152. S. Yadla, P. G. Campbell, R. Chitale, M. G. Maltenfort, P. Jabbour, and A. D. Sharan, "Effect of early surgery, material, and method of flap preservation on cranioplasty infections: a systematic review," Neurosurgery **68**, 1124-1129; discussion 1130 (2011).

153. K. W. Wang, W. N. Chang, C. R. Huang, N. W. Tsai, H. W. Tsui, H. C. Wang, T. M. Su, C. S. Rau, B. C. Cheng, C. S. Chang, Y. C. Chuang, P. C. Liliang, Y. D. Tsai, and C. H. Lu, "Post-neurosurgical nosocomial bacterial meningitis in adults: microbiology, clinical features, and outcomes," Journal of clinical neuroscience : official journal of the Neurosurgical Society of Australasia **12**, 647-650 (2005).

154. G. C. du Moulin, D. Paterson, J. Hedley-Whyte, and S. A. Broitman, "E. coli peritonitis and bacteremia cause increased blood-brain barrier permeability," Brain research **340**, 261-268 (1985).

155. S. R. Dashti, H. Baharvahdat, R. F. Spetzler, E. Sauvageau, S. W. Chang, M. F. Stiefel, M. S. Park, and N. C. Bambakidis, "Operative intracranial infection following craniotomy," Neurosurg Focus **24**, E10 (2008).

156. R. C. Goh, C. N. Chang, C. L. Lin, and L. J. Lo, "Customised fabricated implants after previous failed cranioplasty," J Plast Reconstr Aesthet Surg **63**, 1479-1484 (2010).

157. R. Haas, O. Dortbudak, N. Mensdorff-Pouilly, and G. Mailath, "Elimination of bacteria on different implant surfaces through photosensitization and soft laser. An in vitro study," Clinical oral implants research **8**, 249-254 (1997).

158. M. L. Mason, "Using the laser for implant maintenance," Dentistry today **11**, 74-75 (1992).

159. T. Kato, H. Kusakari, and E. Hoshino, "Bactericidal efficacy of carbon dioxide laser against bacteria-contaminated titanium implant and subsequent cellular adhesion to irradiated area," Lasers in Surgery and Medicine **23**, 299-309 (1998).

160. C. M. Block, J. A. Mayo, and G. H. Evans, "Effects of the Nd:YAG dental laser on plasma-sprayed and hydroxyapatite-coated titanium dental implants: surface alteration and attempted sterilization," The International journal of oral & maxillofacial implants **7**, 441-449 (1992).

161. A. R. Eriksson and T. Albrektsson, "Temperature threshold levels for heat-induced bone tissue injury: a vital-microscopic study in the rabbit," J Prosthet Dent **50**, 101-107 (1983).

162. M. Kreisler, H. Al Haj, and B. d'Hoedt, "Temperature changes at the implant-bone interface during simulated surface decontamination with an Er:YAG laser," The International journal of prosthodontics **15**, 582-587 (2002).

163. A. Geminiani, J. G. Caton, and G. E. Romanos, "Temperature increase during CO(2) and Er:YAG irradiation on implant surfaces," Implant dentistry **20**, 379-382 (2011).

164. X. He, "Thermostability of biological systems: fundamentals, challenges, and quantification," The open biomedical engineering journal **5**, 47-73 (2011).

165. C. H. Contag, P. R. Contag, J. I. Mullins, S. D. Spilman, D. K. Stevenson, and D. A. Benaron, "Photonic detection of bacterial pathogens in living hosts," Mol Microbiol **18**, 593-603 (1995).

166. N. Dinjaski, S. Suri, J. Valle, S. M. Lehman, I. Lasa, M. A. Prieto, and A. J. Garcia, "Near-infrared fluorescence imaging as an alternative to bioluminescent bacteria to monitor biomaterial-associated infections," Acta biomaterialia **10**, 2935-2944 (2014).

167. M. R. Hamblin, D. A. O'Donnell, N. Murthy, C. H. Contag, and T. Hasan, "Rapid control of wound infections by targeted photodynamic therapy monitored by in vivo bioluminescence imaging," Photochemistry and photobiology **75**, 51-57 (2002).

168. S. Sennhenn-Kirchner, S. Klaue, N. Wolff, H. Mergeryan, M. B. von Zepelin, and H. G. Jacobs, "Decontamination of rough titanium surfaces with diode lasers: microbiological findings on in vivo grown biofilms," Clinical Oral Implants Research **18**, 126-132 (2007).

169. E. L. Nussbaum, L. Lilge, and T. Mazzulli, "Effects of low-level laser therapy (LLLT) of 810 nm upon in vitro growth of bacteria: relevance of irradiance and radiant exposure," J Clin Laser Med Surg **21**, 283-290 (2003).

170. S. Kim, J. Kim, W. Lim, S. Jeon, O. Kim, J. T. Koh, C. S. Kim, and H. Choi, "In vitro bactericidal effects of 625, 525, and 425 nm wavelength (red, green, and blue) light-emitting diode irradiation," Photomed Laser Surg **31**, 554-562 (2013).

171. I. Hauser-Gerspach, S. Stubinger, and J. Meyer, "Bactericidal effects of different laser systems on bacteria adhered to dental implant surfaces: an in vitro study comparing zirconia with titanium," Clinical oral implants research **21**, 277-283 (2010).

172. R. O. Darouiche, "Antimicrobial approaches for preventing infections associated with surgical implants," Clinical infectious diseases : an official publication of the Infectious Diseases Society of America **36**, 1284-1289 (2003).

173. S. Stübinger, F. Homann, C. Etter, M. Miskiewicz, M. Wieland, and R. Sader, "Effect of Er:YAG, CO(2) and diode laser irradiation on surface

properties of zirconia endosseous dental implants," Lasers Surg Med **40**, 223-228 (2008).

174. E. L. Nussbaum, L. Lilge, and T. Mazzulli, "Effects of 810 nm laser irradiation on in vitro growth of bacteria: comparison of continuous wave and frequency modulated light," Lasers Surg Med **31**, 343-351 (2002).

175. F. Hillenkamp, "Laser radiation tissue interaction," Health physics **56**, 613-616 (1989).

176. E. L. Nussbaum, L. Lilge, and T. Mazzulli, "Effects of low-level laser therapy (LLLT) of 810 nm upon in vitro growth of bacteria: relevance of irradiance and radiant exposure," Journal of clinical laser medicine & surgery **21**, 283-290 (2003).

177. J. Lee and G. Kaletunç, "Evaluation of the heat inactivation of Escherichia coli and Lactobacillus plantarum by differential scanning calorimetry," Appl Environ Microbiol **68**, 5379-5386 (2002).

178. R. Hibst, R. Graser, M. Udart, and K. Stock, "Mechanism of high-power NIR laser bacteria inactivation," Journal of biophotonics **3**, 296-303 (2010).

179. R. Lubart, A. Lipovski, Y. Nitzan, and H. Friedmann, "A possible mechanism for the bactericidal effect of visible light," Laser therapy **20**, 17-22 (2011).

180. K. Nandakumar, H. Obika, T. Shinozaki, T. Ooie, A. Utsumi, and T. Yano, "Laser impact on bacterial ATP: insights into the mechanism of laser-bacteria interactions," Biofouling **19**, 109-114 (2003).

181. M. Fournier, B. Combes, J. Braga, N. Roberts, and S. Prima, "Mapping the distance between the brain and the inner surface of the skull: interest for the study of fossil endocasts," Am J Phys Anthropol **144**, 137-138 (2011).

182. T. Ando, W. Xuan, T. Xu, T. Dai, S. K. Sharma, G. B. Kharkwal, Y. Y. Huang, Q. Wu, M. J. Whalen, S. Sato, M. Obara, and M. R. Hamblin, "Comparison of therapeutic effects between pulsed and continuous wave 810-nm wavelength laser irradiation for traumatic brain injury in mice," PLoS One **6**, e26212 (2011).

183. W. M. Pardridge, "Blood-brain barrier delivery," Drug Discov Today **12**, 54-61 (2007).

184. S. J. Madsen and H. Hirschberg, "Site-specific opening of the blood-brain barrier," J Biophotonics **3**, 356-367 (2010).

185. H. Hirschberg, F. A. Uzal, D. Chighvinadze, M. J. Zhang, Q. Peng, and S. J. Madsen, "Disruption of the blood-brain barrier following ALA-mediated photodynamic therapy," Lasers Surg Med **40**, 535-542 (2008).

186. H. Hirschberg, M. J. Zhang, H. M. Gach, F. A. Uzal, Q. Peng, C. H. Sun, D. Chighvinadze, and S. J. Madsen, "Targeted delivery of bleomycin to the brain using photo-chemical internalization of Clostridium perfringens epsilon prototoxin," J Neurooncol **95**, 317-329 (2009).

187. Y. Xie, N. Martini, C. Hassler, R. D. Kirch, T. Stieglitz, A. Seifert, and U. G. Hofmann, "In vivo monitoring of glial scar proliferation on chronically implanted neural electrodes by fiber optical coherence tomography," Front Neuroeng **7**, 34 (2014).